

Evidence for Concerted Ring Opening and C-Br Bond Breaking in UV-Excited Bromocyclopropane

Shubhrangshu Pandit,¹ Thomas J. Preston,^{1,b)} Simon J. King,² Claire Vallance² and Andrew J. Orr-Ewing^{1,a)}

¹*School of Chemistry, University of Bristol, Cantock's Close, Bristol, BS8 1TS, UK*

²*Department of Chemistry, University of Oxford, Chemistry Research Laboratory, 12 Mansfield Road, Oxford OX1 3TA, UK*

Photodissociation of gaseous bromocyclopropane via its A-band continuum has been studied at excitation wavelengths ranging from 230 nm to 267 nm. Velocity-map images of ground-state bromine atoms (Br), spin-orbit excited bromine atoms (Br*) and C₃H₅ hydrocarbon radicals reveal the kinetic energies of these various photofragments. Both Br and Br* atoms are predominantly generated via repulsive excited electronic states in a prompt photodissociation process in which the hydrocarbon co-fragment is a cyclopropyl radical. However, the images obtained at the mass of the hydrocarbon radical fragment identify a channel with total kinetic energy greater than that deduced from the Br and Br* images, and with a kinetic energy distribution that exceeds the energetic limit for Br + cyclopropyl radical products. The velocity-map images of these C₃H₅ fragments have lower angular anisotropies than measured for Br and Br*, indicating molecular restructuring during dissociation. The high kinetic energy C₃H₅ signals are assigned to allyl radicals generated by a minor photochemical pathway which involves concerted C-Br bond dissociation and cyclopropyl ring-opening following single UV-photon absorption. Slow photofragments also contribute to the velocity map images obtained at the C₃H₅ radical mass, but corresponding slow Br atoms are not observed. These features in the images are attributed to C₃H₅⁺ from the photodissociation of the C₃H₅Br⁺ molecular cation following two-photon ionization of the parent compound. This assignment is confirmed by 118-nm vacuum ultraviolet ionization studies that prepare the molecular cation in its ground electronic state prior to UV photodissociation.

I. INTRODUCTION:

Absorption of a photon of ultraviolet (UV) light elevates a molecule to an excited state with sufficient internal energy to break chemical bonds. Solar-UV induced fragmentation initiates a wide range of radical chemistry in the Earth's atmosphere, including oxidation of organic compounds in the troposphere and catalytic removal of stratospheric ozone.^{1,2} The photofragmentation of halocarbons to release halogen atoms is significant in determining stratospheric ozone budgets, and organobromine compounds merit particular attention because bromine atoms are more effective than chlorine in catalysing

^{a)} Author for correspondence: a.orr-ewing@bristol.ac.uk.

^{b)} Current address: Institute for Energy Technology, Instituttveien 18, NO-2007 Kjeller, Norway.

ozone destruction.³ Bromine atoms from photodissociation of naturally occurring alkyl bromides are believed to be responsible for 10% of stratospheric ozone loss.⁴

Numerous studies have examined production of Br atoms from UV photodissociation of straight-chain and branched alkyl bromides.^{5–10} These bromoalkanes absorb UV light at wavelengths below 250 nm; the observed broad UV absorption feature is referred to as the A-band, and corresponds to a $\sigma^* \leftarrow \text{Br}(n)$ electronic excitation. The anti-bonding σ^* character in the C-Br bond encourages rapid dissociation into a bromine atom and an alkyl radical.^{5–10} The A band of methyl bromide, a molecule with C_{3v} symmetry, can be decomposed into absorptions to three repulsive electronic states,⁵ denoted by Mulliken¹¹ as 3Q_1 , 1Q_1 and 3Q_0 , and listed in order of increasing energy in the Franck-Condon region. In alkyl bromides with C_s symmetry, the 1Q_1 and 3Q_1 states each split into a pair of A' and A'' states. The transition dipole moment for the $^3Q_0 \leftarrow X$ excitation (with X denoting the ground electronic state) lies parallel to the C-Br bond in CH_3Br , whereas it is perpendicular to the C-Br bond for the $^1Q_1 \leftarrow X$ and $^3Q_1 \leftarrow X$ excitations. Dissociation of CH_3Br on the diabatic 3Q_0 state generates a ground-state methyl radical and spin-orbit excited $\text{Br}^*(^2P_{1/2})$ atom, whereas the 1Q_1 and 3Q_1 states diabatically correlate to CH_3 and a ground spin-orbit state $\text{Br}(^2P_{3/2})$ atom at extended C-Br distances. These asymptotes differ in energy by the Br atom spin-orbit splitting of 3685 cm^{-1} (44.1 kJ mol^{-1}). A conical intersection between the 1Q_1 and 3Q_0 states allows dissociating molecules to switch between these states. Similar dynamics are likely to arise in lower-symmetry alkyl bromides such as bromocyclopropane (BCP), which is the focus of the current study. Figure 1 shows UV absorption spectra of BCP and its isomer allyl bromide (AB), for which additional measurements were made. The figure also includes schematic one-dimensional cuts along the C-Br coordinate for the potential energy surfaces (PESs) responsible for the A-band absorption.

Homolytic bond cleavage can cause ring opening instead of molecular dissociation in cyclic molecules. Experimental and computational studies have examined ring-opening mechanisms of five- and six-membered heterocycles,^{12–14} but definitive experimental signatures are difficult to identify for gaseous molecules. Less attention has been paid to ring-opening in cycloalkyl-containing molecules, the smallest of which are cyclopropyl (Cp) derivatives. Several theoretical studies have considered the mechanism of ring opening in the cyclopropyl radical,^{15–21} and experimentally and computationally determined activation energies lie in the range $80\text{--}92\text{ kJ mol}^{-1}$.^{22–24} The reaction enthalpy for the isomerization of cyclopropyl radical to allyl radical is deduced to be between -95 and -107 kJ mol^{-1} from the experimentally determined heats of formation values of the isomers,^{25,26} and a recent theoretical study showed that an internal rotation of a single methylene group initiates this ring-opening.²¹

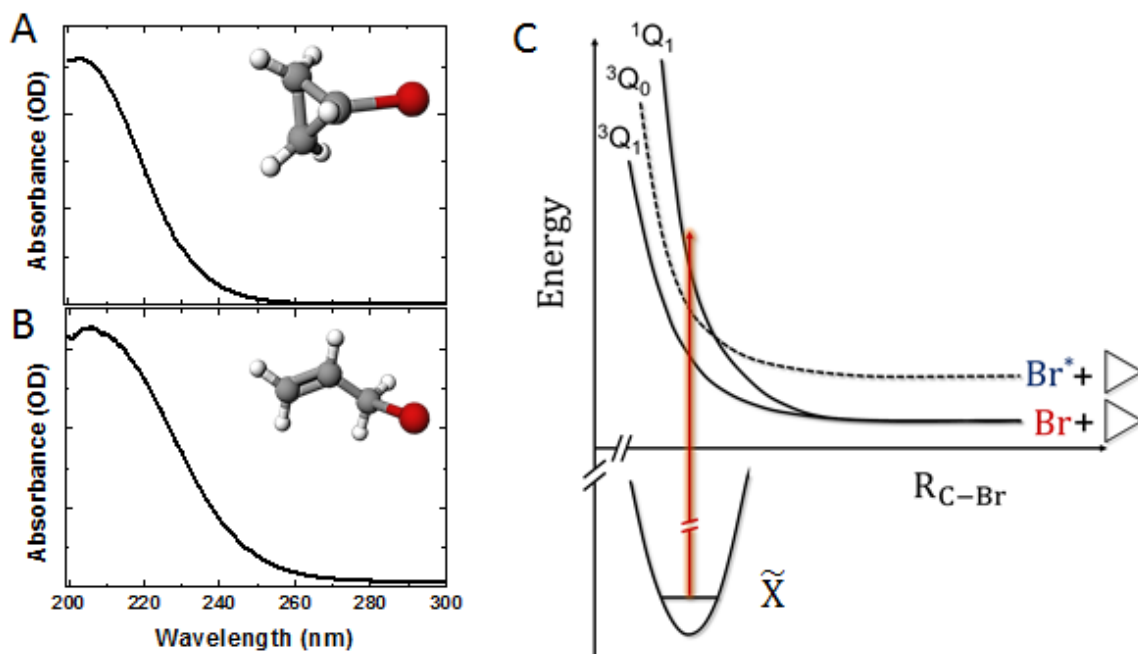


FIG. 1. UV-absorption spectra of (A) bromocyclopropane vapour, (B) allyl bromide vapour. (C) Schematic representation of the low lying potential energy surfaces of bromocyclopropane along the C-Br bond stretching coordinate. The states are labelled with symbols appropriate for CH_3Br , and further splitting of these three excited states in the lower symmetry BCP has not been included.

Carpenter and co-workers proposed an alternative ring-opening mechanism in the photodissociation of iodocyclopropane, involving electron-transfer to a Cp^+I^- ion-pair state, with facile, barrierless opening of the cyclopropyl cation ring to form an allyl cation.²⁷ Heterolytic bond cleavage of the ion-pair state to yield $allyl^+$ and I^- is frustrated by the insufficient available energy, so the molecule returns to a dissociative valence state that leads to homolytic separation. In solution, polar solvents lower the energy of the ion-pair state dissociation limit, with the result that Phillips and co-workers were able to observe allyl cation photofragments by resonance Raman spectroscopy following 228.7 nm excitation of bromocyclopropane in acetonitrile.²⁸ Kropp²⁹ argued that cation production from alkyl-halide photolysis in solution arises from homolytic bond cleavage followed by electron transfer between the radical fragments trapped in a solvent cage, but the mechanism suggested by Carpenter and co-workers presents an alternative explanation. Their proposed ion-pair mediated ring opening and dissociation pathway was motivated by velocity-map imaging (VMI) studies of iodocyclopropane by Houston and co-workers, which revealed I and I^* photofragments with total kinetic energies beyond the thermodynamic limit for the $I + Cp$ radical pathway.²⁷ Photoelectron imaging of the hydrocarbon photofragments from both iodocyclopropane and allyl iodide identified a common photoproduct, providing further evidence for allyl radical formation from both parent molecules.

The current study uses VMI to examine the UV photodissociation of gaseous bromocyclopropane and allyl bromide at photolysis wavelengths in the range 230 - 267 nm. Comparison of images obtained for Br , Br^* and hydrocarbon radicals provides evidence for both ring-retaining cyclopropyl radical and ring-opened allyl radical products from the UV photolysis of

BCP. We compare the images obtained for photodissociation of the neutral molecules with those observed for UV photodissociation of the molecular cations, prepared in their ground electronic states by vacuum UV photoionization.

II. EXPERIMENTAL:

The experimental measurements on neutral bromocyclopropane and allyl bromide photodissociation were performed at the University of Bristol on a VMI machine incorporating a time-of-flight mass spectrometer (TOF-MS). The experimental setup has been reported in detail elsewhere.³⁰ Liquid BCP and AB (both from Sigma Aldrich, 99%) were purified in a glass vacuum line by the freeze-pump-thaw method, and their vapour pressures were used to prepare ~1% samples diluted in 1 bar of argon. The purities of the samples were confirmed by recording IR spectra of the vapours with a PerkinElmer Spectrum Two FT-IR Spectrometer (see Supplemental Material,³¹ Figure S.1). The A-band absorptions were characterized by UV-visible absorption spectroscopy using a Thermo Scientific GENESYS 10S UV-VIS Spectrometer. Expansion of the dilute gas samples through a pulsed nozzle (Parker Hannifin Series 9, 10 Hz repetition rate) and collimation of the resulting expansion with a 1-mm diameter skimmer generated a molecular beam of the selected bromo-compound seeded in argon. The expansion was coaxial with the time-of-flight axis, and the vacuum in the chamber was maintained at 10^{-7} Torr during measurements.

BCP and AB were photolysed at selected wavelengths in the range 230 - 245 nm and at 267 nm. The former range of photolysis wavelengths was generated by a pulsed dye laser (Sirah PRSC-G-24 using Coumarin 480 dye) pumped by the third harmonic of a pulsed Nd:YAG laser (Spectra-Physics Quanta-Ray GCR-230). The dye-laser fundamental output was frequency doubled in a BBO crystal to generate 0.2 mJ per pulse of UV photolysis light. Br and Br* were detected using (2+1) resonance enhanced multiphoton ionization (REMPI) at 266.6 nm ($4p\ ^2P_{3/2} \rightarrow 5p\ ^4P_{3/2}$) and 266.67 nm ($4p\ ^2P_{1/2} \rightarrow 5p\ ^4S_{3/2}$) respectively. The probe laser pulses were generated by a pulsed dye laser (Sirah Cobra Stretch, Coumarin 500 dye) pumped by the third harmonic of a second Nd:YAG laser (Continuum Surelite SLIII-10). The light produced by the dye laser was frequency doubled by a KDP crystal, before being focused by a 25 cm focal length lens into the chamber approximately 10 mm in front of the repeller plate of the TOF MS. The typical probe laser energy was 1 mJ per pulse. The Doppler-broadened absorption lines of Br and Br* necessitated a scan of the probe wavelength range to image all Br or Br* fragments with the same efficiency. The two-colour signals dominated probe-laser-only signals under our experimental conditions, but we were also able to accumulate images when the probe laser was used as a source of both photolysis and probe light in studies of the 267-nm photolysis of BCP and AB.

Hydrocarbon radicals with mass 41 g mol^{-1} (C_3H_5) were selected in the TOF-MS and imaged following multiphoton ionization. Because the allyl radical has a known (1+1) REMPI scheme at wavelengths around 240 nm, ionization was performed with the probe laser tuned in the range 230 nm–250 nm. The same laser pulse was also used to photolyse the parent bromocyclopropane or allyl bromide. In these one-colour measurements, pulse energies from the frequency-doubled dye laser output were $\leq 1.5 \text{ mJ}$.

The laser beams propagated perpendicular to the molecular beam and TOF-MS axis in all the measurements of neutral-molecule photodissociation. Both the pump and probe laser pulses were linearly polarized, with their electric field vectors aligned parallel to the face of the position-sensitive detector. A time delay of 30–50 ns was set between pump and probe pulses in the two-colour experiment to minimize unwanted background signals.

The VMI ion optics were configured for DC-slice velocity-map imaging of the Br^+ or C_3H_5^+ ions onto a detector consisting of a pair of 75-mm diameter microchannel plates coupled to a P47 phosphor screen. A CCD camera observing the rear of the phosphor screen captured points of impact of the ions on the MCPs, at arrival times corresponding to either $m/z = 79$ ($^{79}\text{Br}^+$) or 41 (C_3H_5^+) ions, with a gated detection duration of 100 ns for each mass. Conversion of experimental images to radial velocity distributions used pixel-to-speed conversion factors calibrated by multi-photon excitation of O_2 at 224.999 nm,³² Cl atoms from the 355-nm photolysis of Cl_2 , and Br atoms from the 532-nm photolysis of Br_2 .

A second set of experiments examined the photodissociation of molecular cations prepared by one-photon VUV ionization of the parent neutral molecules. These experiments used a VMI apparatus at the University of Oxford, which has been described previously.³³ A gas mixture of ~8% BCP or AB seeded in 1 bar of argon was expanded through a pulsed valve (Parker Hannifin Series 9), operating at 10 Hz. The molecular beam was skimmed prior to entry to the reaction chamber and was intersected by VUV laser radiation of wavelength 118.2 nm. This VUV light was generated by tripling the tightly focused 355 nm third harmonic of a Nd:YAG laser (Continuum Surelite I, ~10–20 mJ per 5 ns pulse) in a cell containing a phase-matched mixture of Xe and Ar (both BOC) in a ratio of 1:11.¹⁰ The residual 355-nm light was not separated from the 118 nm light, and was exploited to photolyse some of the cations. Shorter UV wavelength photolysis experiments on the cations used 230 – 240 nm laser pulses with energies of 0.7 – 1.2 mJ per pulse, which were produced by frequency-doubling the output of a Nd:YAG-pumped dye laser (Continuum Surelite II and Sirah Cobra Stretch). The linear polarization vectors of all the laser beams were aligned parallel to the face of the position-sensitive detector. The time delay between the VUV pump and UV photolysis laser pulses was 20 ns.

The position-sensitive detector consisted of a triple-stacked set of 40-mm-diameter microchannel plates coupled to a P47 phosphor screen. Velocity-map images were recorded for all masses using a PImMS1 multimass-imaging camera.³⁴ The

camera has been described in detail previously.³⁵ On each time-of-flight cycle, the camera records the position and arrival time of each detected ion, with a time resolution of 12.5 ns. Data were acquired over 10 000 laser pump-probe cycles. The images were processed using a software suite written in-house.

The slower fragments in allyl images from neutral dissociation of AB and BCP in the Bristol experiments were too slow for effective slicing using the instrument's minimum detector gate width of 100 ns. Hence, a partial slicing analysis method was used to extract the velocity distributions of the slower allyl fragments after pixel-density correction over the whole velocity range.³⁶ Cationic dissociation of AB⁺ and BCP⁺ also gives fragments with low kinetic energies, and the same velocity distribution reconstruction routine was therefore used to analyse data from the Oxford experiments. A five-adjacent-point averaging algorithm reduced the noise in kinetic energy distribution plots.

III. RESULTS AND DISCUSSION:

The results obtained by imaging the Br, Br* and C₃H₅ hydrocarbon radical photoproducts from bromocyclopropane are presented in Section III.A. The REMPI and imaging of the hydrocarbon radical used wavelengths appropriate for allyl radical detection, and we confirmed that we could successfully image allyl radicals at this wavelength by carrying out studies of allyl bromide photolysis. The results of these AB measurements, and of imaging the Br and Br* co-fragments, are presented in Section III.B and Supplemental Material.³¹ Images at the C₃H₅⁺ mass show additional features that were tentatively assigned to dissociation of the molecular cations formed by multiphoton ionization at the photolysis laser wavelength. These assignments were tested by performing VUV ionization experiments that prepared the cations prior to photodissociation, the results of which are presented in Section III.C. These measurements also confirm that the cation photodissociation does not interfere with the signals interpreted as originating from the neutral alkyl bromide compounds.

A. VMI of photofragments from bromocyclopropane

1. Br and Br* photofragment images from bromocyclopropane photolysis

Figure 2 shows velocity-map images of Br and Br* fragments from the UV photodissociation of bromocyclopropane at four different wavelengths in the range 230-245nm. Measurements were also made for photolysis at the probe laser wavelength of 267 nm. In principle, the sliced images require no further processing to extract speed and angular distributions, although we chose to symmetrize them about the central vertical and horizontal axes to improve the signal-to-noise ratio. The centre of each

image corresponds to zero recoil velocity of the photofragments in the centre-of-mass frame. The linear polarization vector of the photolysis laser is parallel to the vertical axis of the image. The angular distributions were fitted to the expression

$$I(\theta) \propto 1 + \beta P_2(\cos\theta). \quad (1)$$

to obtain values of β , the anisotropy parameter.³⁷

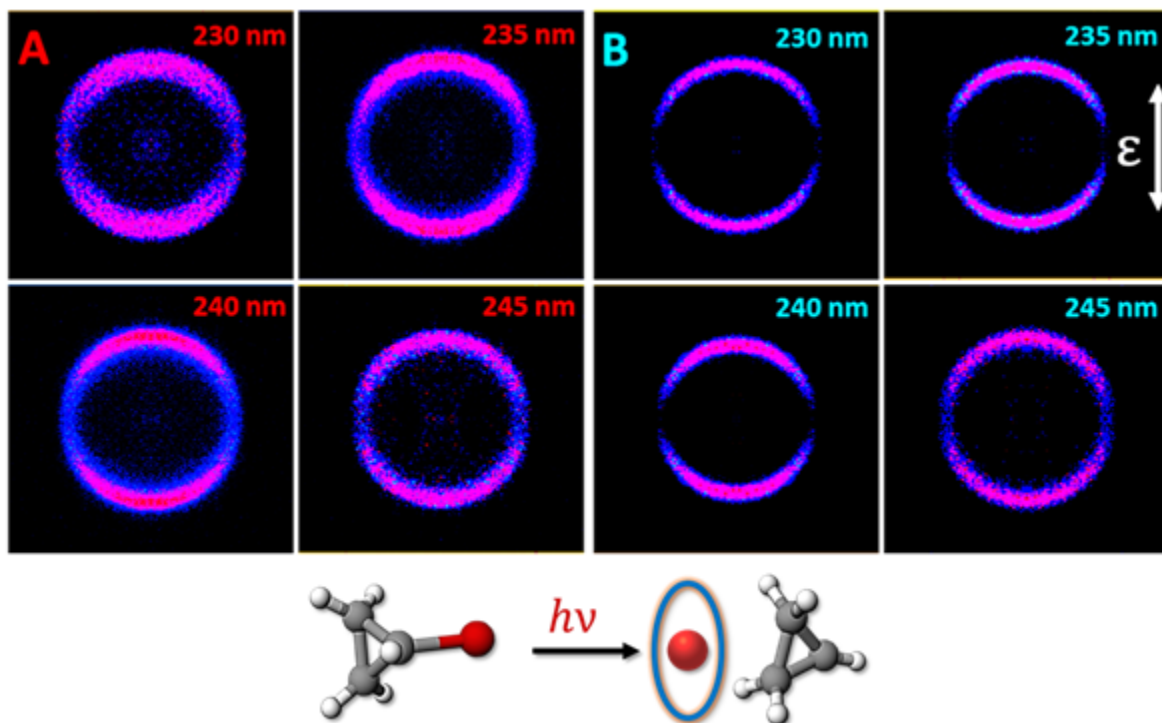


FIG. 2. Time-sliced velocity map images of (A) Br ($^2P_{3/2}$) (left) and (B) Br* ($^2P_{1/2}$) (right) photofragments from bromocyclopropane at four different photolysis wavelengths. The photolysis laser polarization vector is aligned parallel to the vertical axis of these images, as shown by the double-headed arrow in the upper right corner panel. A schematic representation of the photochemistry is shown at the bottom, highlighting the imaged fragment.

Here, θ is the angle between the photolysis laser polarization axis and the recoil velocity vector of the Br or Br* fragment, and $P_2(\cos \theta)$ is a second-order Legendre polynomial. All of the excited states giving rise to the A-band are repulsive along the C-Br bond, which defines the direction of axial recoil for the photofragments.^{38–40} Excitation to the 3Q_0 state gives a limiting value of $\beta = +2$, whereas the limiting value is $\beta = -1$ for excitation to the 3Q_1 and 1Q_1 states. Values of β intermediate between these limits indicate either mixed excitation or significant geometry changes during dissociation. We adopt the labels appropriate for states of CH₃Br, and these states are shown schematically in Figure 1(C). The anisotropy parameter values obtained at five different photolysis wavelengths are summarized in Table I.

TABLE I: Anisotropy parameters for Br and Br* photofragments from bromocyclopropane at various photolysis wavelengths.

Bromocyclopropane Fragment	β				
	230 nm	235 nm	240 nm	245 nm	267 nm
Br	0.80±0.04	0.94±0.03	1.31±0.01	0.75±0.05	1.11±0.01
Br*	1.48±0.06	1.68±0.02	1.51±0.05	1.61±0.02	0.62±0.01

The 3Q_1 and 1Q_1 states that arise in molecules with C_{3v} symmetry split into $[2A' 1A'']$ and $[4A' 2A'']$ pairs of states in the C_s point group of bromocyclopropane, with the 3Q_0 state becoming the $3A'$ state.^{6,9,10} However, we expect these splittings to be small.^{6,9} Therefore, we consider only three excited states to contribute to the A-band photodissociation, and retain the Mulliken 3Q_1 , 1Q_1 , 3Q_0 notation in order to facilitate comparison with methyl bromide. The transition dipole moment for excitation to the 3Q_0 state lies close to parallel to the C-Br bond (within 6° according to our optimized structure of BCP using the m062x density functional⁴¹ and Dunning's aug-cc-pVDZ basis set⁴²), whereas the transition dipole is close to perpendicular to the C-Br bond for excitation to the 3Q_1 and 1Q_1 states. Diabatic dissociation on the 3Q_1 and 1Q_1 states produces Br($^2P_{3/2}$) atoms, while the diabatic 3Q_0 state produces Br*($^2P_{1/2}$), in both cases partnered by a ground-state cyclopropyl radical. These symmetry considerations and state correlations predict $\beta(\text{Br}) = -1$ and $\beta(\text{Br}^*) = 2$ if the photodissociation is prompt and no flux transfer occurs between states during dissociation. The excited-state lifetimes are expected to be ~ 100 fs, which is much shorter than the rotational period of the molecule.^{5,6} The anisotropy parameter values in Table I therefore indicate coupling between the 1Q_1 and 3Q_0 states during dissociation, giving both parallel ($\beta_{\parallel} = +2$) and perpendicular ($\beta_{\perp} = -1$) components to the measured Br and Br* images. The relative contributions can be determined using the following expressions:

$$\beta(\text{Br}) = a\beta_{\parallel} + b\beta_{\perp}. \quad (2)$$

$$\beta(\text{Br}^*) = c\beta_{\parallel} + d\beta_{\perp}. \quad (3)$$

Here, a is the fraction of Br generated through parallel band excitation to the 3Q_0 state, and b is the fraction from perpendicular band excitation to the 3Q_1 and 1Q_1 states. Similarly c and d are the fractions of Br* resulting from excitation to the 3Q_0 and 1Q_1 states respectively. Table II presents these fractions obtained at different photolysis wavelengths. This analysis assumes that the angular anisotropy is exclusively determined by the photofragment recoil velocity distribution, and is not affected by angular momentum polarization effects resulting from coherent excitation of more than one electronically excited state.⁴³ The

Supplemental Information contains a more detailed analysis of the angular anisotropies, which supports our assumption of only weak influence from the coherent nature of the excitation process.

TABLE II: Parallel and perpendicular excitation fractions for the Br and Br* fragmentation channels from bromocyclopropane at various photolysis wavelengths.

BCP	Transition	Parallel or perpendicular transition fraction				
Fragment		230 nm	235 nm	240 nm	245 nm	267 nm
Br	parallel	0.60±0.01	0.65±0.01	0.77±0.01	0.58±0.02	0.70±0.01
	perpendicular	0.40±0.01	0.35±0.01	0.23±0.01	0.42±0.02	0.30±0.01
Br*	parallel	0.83±0.02	0.89±0.01	0.84±0.01	0.87±0.01	0.54±0.01
	perpendicular	0.17±0.02	0.11±0.01	0.16±0.01	0.13±0.01	0.46±0.01

The values in Table II indicate that more than 80% of Br* originates from initial excitation to the 3Q_0 state of bromocyclopropane, with the remainder arising from initial excitation to the 1Q_1 state followed by crossing via the conical intersection to the 3Q_0 state, or perhaps forming via other more complicated pathways. Ground-state Br production is also mostly via a parallel transition to the 3Q_0 state, in this case followed by transfer via the conical intersection to the 1Q_1 state. This analysis implies a larger absorption cross section for excitation to the 3Q_0 state compared with excitation to the 3Q_1 and 1Q_1 states in the wavelength region studied, which is consistent with decomposition of the A-band of CH₃Br.⁵ The transfer between states appears to be more significant following 267 nm excitation, in accord with similar results from other alkyl halides^{7–9} and Landau-Zener model analysis:^{44,45} transfer between diabatic electronic states is more efficient at the lower photofragment recoil velocities associated with longer excitation wavelengths.

2. VMI of hydrocarbon radicals from bromocyclopropane photolysis

Velocity-map images of $m/z = 41$ hydrocarbon fragments from the photolysis of bromocyclopropane at four different wavelengths from 230 – 245 nm are shown in Figure 3. In these one-colour images, a single laser pulse both photolysed and ionized the neutral radical photofragments. Two components with very different velocity distributions are evident in the images. The slower fragments peak in intensity near the image centre, and we argue in Section III.C that they correspond to fragments from dissociation of the BCP⁺ cation. The faster photofragments contributing to the outer rings in the images are C₃H₅ radicals

formed in coincidence with bromine atoms by photolysis of the neutral parent molecule. The hydrocarbon radical fragments associated with Br and Br* production channels should have different translational energy distributions, but a distribution of internal energies in the radical, together with the non-state-specific ionization scheme employed, prevents full resolution of separate rings in the images. We therefore analysed the angular anisotropy of the outer rings in the images, in terms of the anisotropy parameter β , in four different total kinetic energy release (TKER) ranges. The results are summarized in Table III.

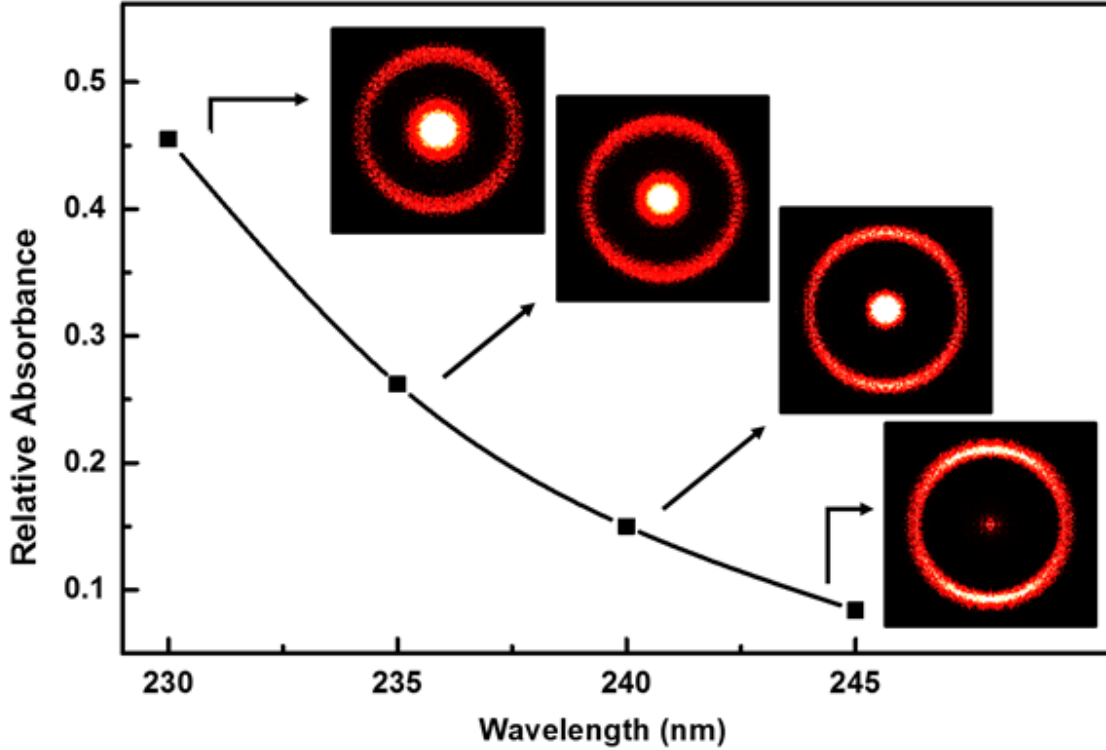


FIG. 3. Time-sliced velocity map images of C_3H_5 photofragments from bromocyclopropane at four different photolysis wavelengths. The photolysis laser polarization vector is oriented parallel to the vertical axis of these images. The graph shows the relative absorbance of BCP at the four observation wavelengths.

TABLE III: Total kinetic energy release dependence of the anisotropy parameters for the $m/z = 41$ hydrocarbon radical photofragments from bromocyclopropane at different photolysis wavelengths.

Wavelength (nm)	$\beta(TKER)^a$ TKER range (kJ mol^{-1})				$\langle\beta\rangle^b$
	80-100	100-120	120-140	140-160	
230	0.54	0.51	0.55	0.29	0.51 ± 0.2
235	0.54	0.51	0.61	0.38	0.54 ± 0.2
240	0.50	0.64	0.60	0.32	0.58 ± 0.1

245	0.66	0.81	0.57	0.30	0.70±0.1
-----	------	------	------	------	----------

^aUncertainties in β for each TKER range are < 7%.

^bAnisotropy parameter averaged over the whole TKER range for the outer ring in each image.

The anisotropy parameter decreases towards the highest photofragment TKERs, consistent with the expectation that the faster hydrocarbon radicals form with $\text{Br}(^2\text{P}_{3/2})$ atoms, which show lower spatial anisotropy than spin-orbit excited $\text{Br}^*(^2\text{P}_{1/2})$ atoms (Table I). However, the anisotropy parameters of the observed hydrocarbon radicals are smaller than those measured by detecting either Br or Br^* fragments. The β values in Table III cannot therefore be expressed as a weighted average of $\beta(\text{Br})$ and $\beta(\text{Br}^*)$ values, as would be expected if the radical is a co-product from direct C-Br bond dissociation in bromocyclopropane. The implications are threefold: one, that the observed hydrocarbon radical fragment is generated via a pathway that is distinct from cyclopropyl + Br/ Br^* production; two, that the radical fragments imaged in our experiments are not cyclopropyl radicals; and three, that this channel is a minor pathway because it does not imprint strongly on the Br and Br^* images. The reduced β values can be explained by a geometric change, such as ring-opening, in which the orientation of the C-Br bond alters in synchrony with its dissociation.

3. Comparison of TKER distributions obtained from Br, Br^* and C_3H_5 images

The analysis of the Br, Br^* and hydrocarbon radical images from bromocyclopropane photolysis has so far concentrated on the spatial anisotropies of the recoiling photofragments. The image analysis also provides TKER distributions from the speed distributions for each fragment at the different photolysis wavelengths used in our measurements. These distributions are presented in Figure 4, and compared to the thermodynamic limits expected from the bond dissociation energy of BCP (listed in Table IV) and the spin-orbit splitting of the Br atom. These thermodynamic limits are calculated for a cyclopropyl radical co-fragment with no internal energy.

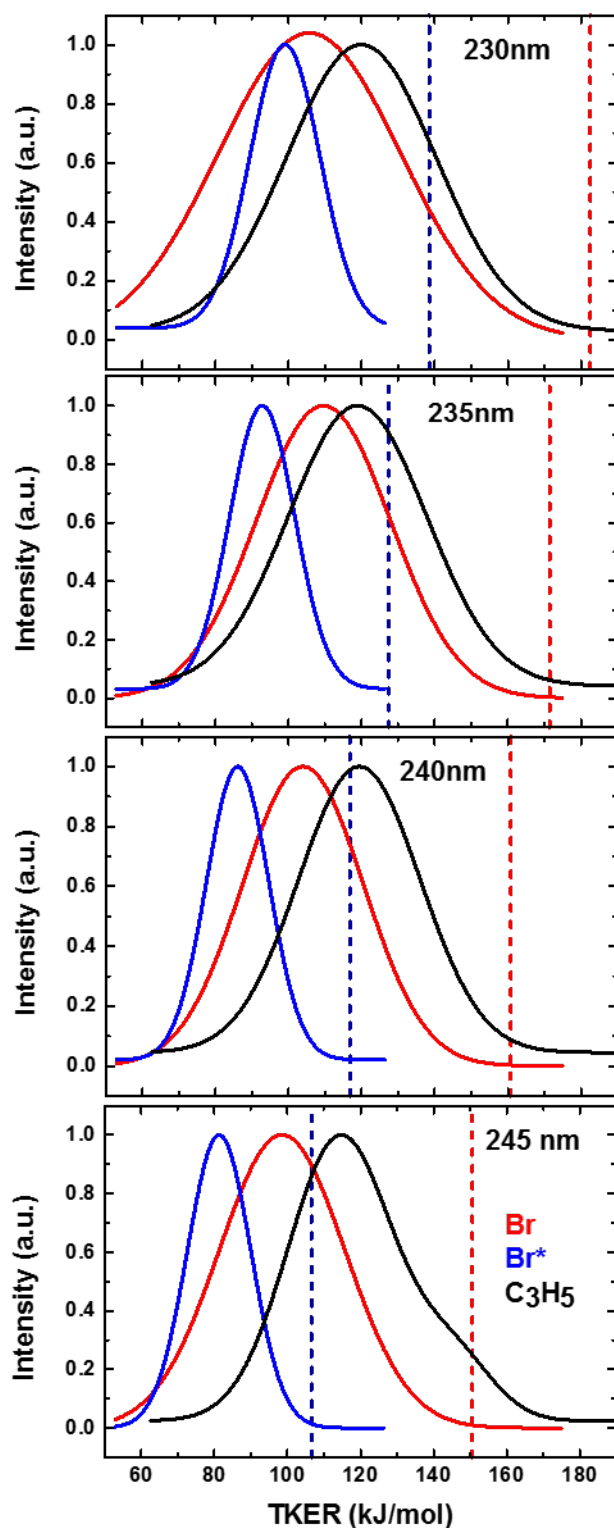


FIG. 4. Total kinetic energy release distributions of photofragments from bromocyclopropane at four different photolysis wavelengths. The red curve is from analysis of Br ($^2P_{3/2}$) images, the blue curve is from Br* ($^2P_{1/2}$) images and the black curve is from C₃H₅ images. The vertical dashed lines represent the thermodynamic limits for the Br (red) or Br* (blue) and Cp (cyclopropyl) radical (with no internal energy) channel. A small fraction of products has total kinetic energies beyond the thermodynamic limit. At all four photolysis wavelengths, the C₃H₅ image TKER extends beyond the limit of possible weighted averages of Br and Br* TKER distributions.

TABLE IV: Reaction enthalpies of different dissociation channels for BCP and AB, and for cyclopropyl radical (Cp) ring opening.

Molecule	Dissociation process	Reaction enthalpy
		/ kJ mol ⁻¹
Bromocyclopropane	BCP → Cp + Br	337.9 ^a
	BCP → Cp + Br [*]	381.9 ^(a)
	BCP → Allyl + Br	225.6 ± 3.0 ^b
	BCP → Allyl + Br [*]	269.6 ± 3.0 ^b
	Cp → Allyl	-112.3 ± 3.0 ^b
Allyl bromide	AB → Allyl + Br	235.2 ± 3.0 ^b
	AB → Allyl + Br [*]	279.2 ± 3.0 ^b

^aTo calculate reaction enthalpies, ΔH_f^0 values for BCP and Cp were taken from ref. 27 and ref. 46 respectively and ΔH_f^0 values of Br and Br^{*} were taken from the *NIST Chemistry WebBook*.⁴⁷

^b ΔH_f^0 of allyl radical was taken from ref. 41 and for AB was taken from ref. 42.

The TKER distributions deduced for Br and Br^{*} fragments lie within the thermodynamic limit for Br + Cp formation, and the Br^{*} distributions peak at lower TKER, as expected for the spin-orbit excited atomic products. The TKER distributions fit well to single Gaussian functions, implying that Br and Br^{*} are generated by direct photodissociation of bromocyclopropane via repulsive PESs.⁴⁸ The peak values from these fits scale linearly with photolysis photon energy, which is indicative of a one-photon dissociation process if a constant fraction of the energy available to the products enters product translational motion over the wavelength range studied. In contrast, the peaks of the TKER distributions derived from analysis of the $m/z = 41$ images (Figure 4) are insensitive to the wavelength of the UV excitation laser (see Supplemental Material,³¹ section S.5).

Table V: Average fraction $\langle f_t \rangle$ of the total available energy going into the translational degrees of freedom of both photoproducts from bromocyclopropane.

Bromocyclopropane	$\langle f_t \rangle^a$			
Fragment	230 nm	235 nm	240 nm	245 nm
Br	0.58	0.64	0.65	0.65
Br [*]	0.71	0.73	0.74	0.76

^aUncertainties in $\langle f_t \rangle$ are <1% for both Br and Br^{*} fragments at all photolysis wavelengths.

Table V summarizes the average fractions of the total available energy found in product translation. The balance of energy not observed as TKER is accounted for by internal excitation of the radical co-fragment. Approximately 35 – 42% of

the available energy is deposited in internal motions of the Cp radical for the Br channel, with a smaller fraction for the Br* channel. A simple impulsive model of the dissociation predicts that this internal energy fraction will be ~60%.⁴⁹

The difference between the centres of the TKER distributions deduced from Br and Br* images is ~20 kJ mol⁻¹, which is smaller than the spin-orbit splitting of the bromine atoms. The TKER distributions plotted in Figure 4 are also broader for the Br than the Br* forming channel (see Figure S. 5 in the Supplemental Material³¹). These above observations and $\langle f_i \rangle$ values indicate that the hydrocarbon radicals are more highly internally excited when formed in coincidence with Br than Br*. This contrast is greatest for photolysis at 230 nm, which suggests the onset of greater vibrational excitation of the radical. Hess *et al.*⁵⁰ observed similar behaviour for CH₃Br photolysis, and argued that dissociation on the steeper ¹Q₁ state correlating to Br(²P_{3/2}) gave the CH₃ radical less time to relax its geometry than dissociation to Br* on the shallower ³Q₀ PES. Morokuma and co-workers^{51,52} provided further insights from their calculations for CH₃I dissociation. The CH₃ experiences a significant geometry change on passage through the conical intersection between the ³Q₀ and ¹Q₁ surfaces, and a similar pathway accounts for most of the Br atoms observed in our measurements for bromocyclopropane. Geometry changes in the Cp moiety associated with dynamics at the conical intersection will channel energy into the internal modes of the cyclopropyl radical fragment.

The total kinetic energy distributions deduced from analysis of hydrocarbon-radical images from bromocyclopropane are compared with the distributions derived from Br and Br* images in Figure 4. A striking observation from the comparisons is that the TKER distributions deduced from images of the hydrocarbon radical fragment (Figure 3) peak at higher energy than the corresponding distributions deduced from images of either Br or Br* atoms (Figure 2). The imaged radical cannot be cyclopropyl because its TKER distribution should be a weighted average of the distributions derived from Br and Br* products, with the weighting reflecting the Br*/Br branching ratio. The maximum of this averaged TKER distribution would lie between the maxima of the two component distributions. Therefore, there must be another C₃H₅ photoproduct formed by a different mechanism; for this additional pathway, the total energy available to the probed hydrocarbon radicals must be greater than that available to the Br and Br* fragments that make up the majority of the signals captured in the images in Figure 2.

We recall that we have chosen an ionization wavelength for the hydrocarbon photoproducts that is appropriate for REMPI detection of allyl radicals, and propose that the $m/z = 41$ fragments imaged in Figure 3 are therefore exclusively allyl radicals. The enthalpy changes on formation of allyl radical and Br or Br* from BCP are 225.6 kJ mol⁻¹ and 269.6 kJ mol⁻¹, respectively (see Table IV), and formation of the allyl radical from BCP photolysis therefore provides an additional 112.3 kJ mol⁻¹ of energy to the photofragments compared to Cp radical formation. This additional energy can account for the higher TKERs observed when imaging at $m/z = 41$ if we probe allyl fragments and our REMPI detection is blind to the cyclopropyl

radicals. The ionization energies of the two radicals are similar (786 kJ mol^{-1} for allyl⁵³ and 790 kJ mol^{-1} for cyclopropyl⁵⁴), but we are not aware of reports of REMPI detection schemes for cyclopropyl radical in this probe wavelength region.

The preceding arguments implicitly assume that allyl radical formation is a minor channel, albeit the one we probe when imaging $m/z = 41$ ions. The majority of Br and Br* atoms instead form alongside a cyclopropyl radical, giving TKER distributions dominated by this latter pathway when we image Br and Br*. We estimate a conservative upper limit to the allyl radical forming channel of 5% on the basis that we cannot see momentum matched Br and Br* atoms in their corresponding velocity map images above our experimental noise levels. The TKER distribution derived from the C_3H_5 images peaks at no more than 20 kJ mol^{-1} above that deduced from Br images, indicating that less than 20% of the 112 kJ mol^{-1} extra available energy in the proposed ring-opening channel enters product translation. This deduction is consistent with a substantial geometry change in the C_3H_5 radical moiety inducing vibrational excitation of the allyl product.

For some or all of the excess energy of the isomerization to appear in the TKER of the separating fragments, the ring-opening to allyl and the C-Br bond breaking must be a *concerted* processes. An alternative stepwise mechanism, in which the ring opens after the C-Br bond breaks and the fragments have separated, cannot impart the greater kinetic energy to the two fragments that we observe in our measurements. Moreover, the unimolecular rate of ring-opening of a separated cyclopropyl radical will increase with increasing internal energy, corresponding to a smaller amount of energy remaining for translational motion of the products. These energy-balance arguments therefore predict low product TKERs in the case of sequential C-Br bond cleavage and cyclopropyl ring opening.

The images in Figure 3 show two distinct TKER components, but in Figure 4 and the discussion presented so far we have concentrated on the faster component. The low TKER component, peaking at zero kinetic energy, is not seen in the Br and Br* images, or in the TKER distributions deduced from them, but is evident in images obtained at the hydrocarbon radical mass. Further discussion of this low-TKER component is deferred to Section III.C, where we argue that it derives from photolysis of the bromocyclopropane cation. The cation photolysis favours formation of C_3H_5^+ , which is imaged directly. Images collected for Br and Br* atoms used smaller photolysis laser pulse energies, with lower propensities for multiphoton ionization of the parent molecule, and are therefore less prone to contamination by bromocyclopropane cation fragmentation.

B. Velocity-map imaging of photofragments from allyl bromide

Complementary VMI studies of allyl bromide photolysis were undertaken at the same photolysis wavelengths as used in our measurements for bromocyclopropane. These additional measurements were performed for two main reasons. One was to confirm that we could detect allyl photofragments using one-colour photolysis followed by REMPI at wavelengths from 230 –

245 nm, in order to support our hypothesis of allyl radical detection from bromocyclopropane. The second was to ensure that our BCP images were not contaminated by signals from AB, present either as a minor impurity in our BCP samples, or produced by unintentional isomerization in our gas-handling system supplying the pulsed nozzle. We note that FTIR studies of the bromocyclopropane and allyl bromide indicated no discernible contamination of either sample (see Supplemental Material Figure S.1³¹).

Table VI: Anisotropy parameters and calculated parallel and perpendicular fractions of Br and Br* photofragments from allyl bromide at four different photolysis wavelengths.

Wavelength	β^a		Parallel and Perpendicular Transition Fractions			
	Br	Br*	Br		Br*	
			Parallel	Perpendicular	Parallel	Perpendicular
230 nm	0.66	1.34	0.53	0.47	0.78	0.22
235 nm	1.02	1.70	0.67	0.33	0.90	0.10
240 nm	0.77	1.24	0.59	0.41	0.75	0.25
245 nm	0.60	0.92	0.53	0.47	0.64	0.36

^aAnisotropy parameters averaged over the whole TKER range, with fitting uncertainties <2% .

Velocity-map images of Br and Br* from the photolysis of allyl bromide are shown in Figure S.2 for photolysis wavelengths of 230, 235, 240 and 245 nm. The Br and Br* images show overlapping double rings with spatial anisotropies summarized in Table VI, and are commensurate with a preference for a parallel transition to the ³Q₀ state, as deduced for CH₃Br photolysis in its A-band. The TKER distributions of the photofragments for the Br and Br* channels are bimodal in nature, which is consistent with previous work by Ji *et al.*⁵⁵, who provided an interpretation of the photochemistry. However, we concentrate here on the images for the co-fragment C₃H₅ radical. These are shown in Figure 5.

Table VII: Total kinetic energy release dependence of the anisotropy parameters for the allyl radical photofragments from allyl bromide at different photolysis wavelengths.

Wavelength (nm)	β -parameter TKER range (kJ mol ⁻¹)			$\langle\beta\rangle^a$
	80-110	110-140	140-170	
230	0.24	0.33	0.35	0.30±0.1
235	0.30	0.36	0.33	0.33±0.1
240	0.35	0.37	0.36	0.35±0.1
245	0.58	0.54	0.37	0.51±0.2

^aAnisotropy parameter averaged over the whole TKER range for the faster ring in each image.

All the images obtained at $m/z = 41$ show a ring corresponding to high kinetic energy C_3H_5 radicals, assumed hereafter to be allyl, but the images at 230 and 235 nm also contain a central, slow component. We conducted an analysis of the speed dependence of the anisotropies of the outer rings similar to that described in Section III.A, and the resulting anisotropy parameters are reported in Table VII for different TKER intervals. Similarities with the anisotropy parameters presented in Table III for the hydrocarbon radical product of BCP photolysis suggest that we are observing common radical photofragments deriving from similarly structured intermediates. However, there is a systematic difference in β -values at all photolysis wavelengths (see section S.4 of the Supplemental Material³¹).

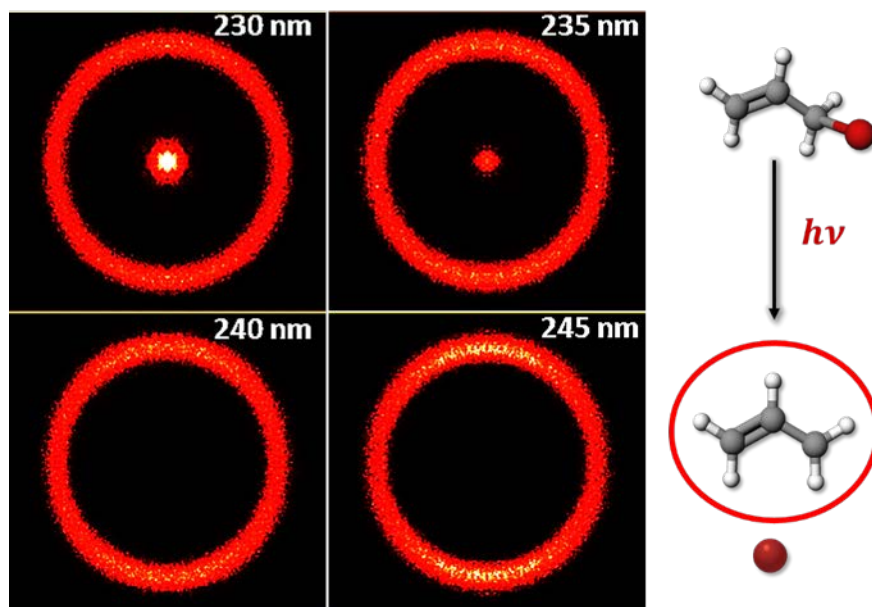


FIG. 5. Sliced velocity map images of $m/z = 41$ photofragments from allyl bromide at four different photolysis wavelengths. The photolysis laser polarization vector is oriented parallel to the vertical axis of these images. A schematic representation of the photochemistry is shown in the right hand panel. The red ring highlights that the velocity map images are of allyl radical photofragments.

The TKER distributions obtained from analysis of the outer rings in all the allyl bromide photolysis images are shown in Figure 6. The observation of a low-TKER component in the $m/z = 41$ images only for wavelengths of 230 and 235 nm is indicative of photolysis of the allyl bromide cation: the energy required for the ionization of allyl bromide is $\sim 982 \text{ kJ mol}^{-1}$,^{56,57} and the threshold wavelength below which two-photon ionization can occur is therefore $\sim 243 \text{ nm}$. A third photon dissociates AB^+ into allyl $^+$ and Br/Br * fragments, with low recoil velocities.¹⁰ This low TKER is consistent with observations from our cation photodissociation experiments, and we return to discussion of our assignment in Section III.C.

Comparison of the TKER distributions of the faster moving allyl radicals with those deduced from analysis of Br and Br * images in Figure 6 shows peaks that lie within the envelope of these latter two distributions. This outcome is expected because the allyl radicals form with a mixture of Br and Br * co-products. The peaks of the TKER distributions scale linearly

with photon energy, and the fraction of the total available energy entering translational degrees of freedom is 45-47%. This fraction is deduced using bond dissociation energies listed in Table V.

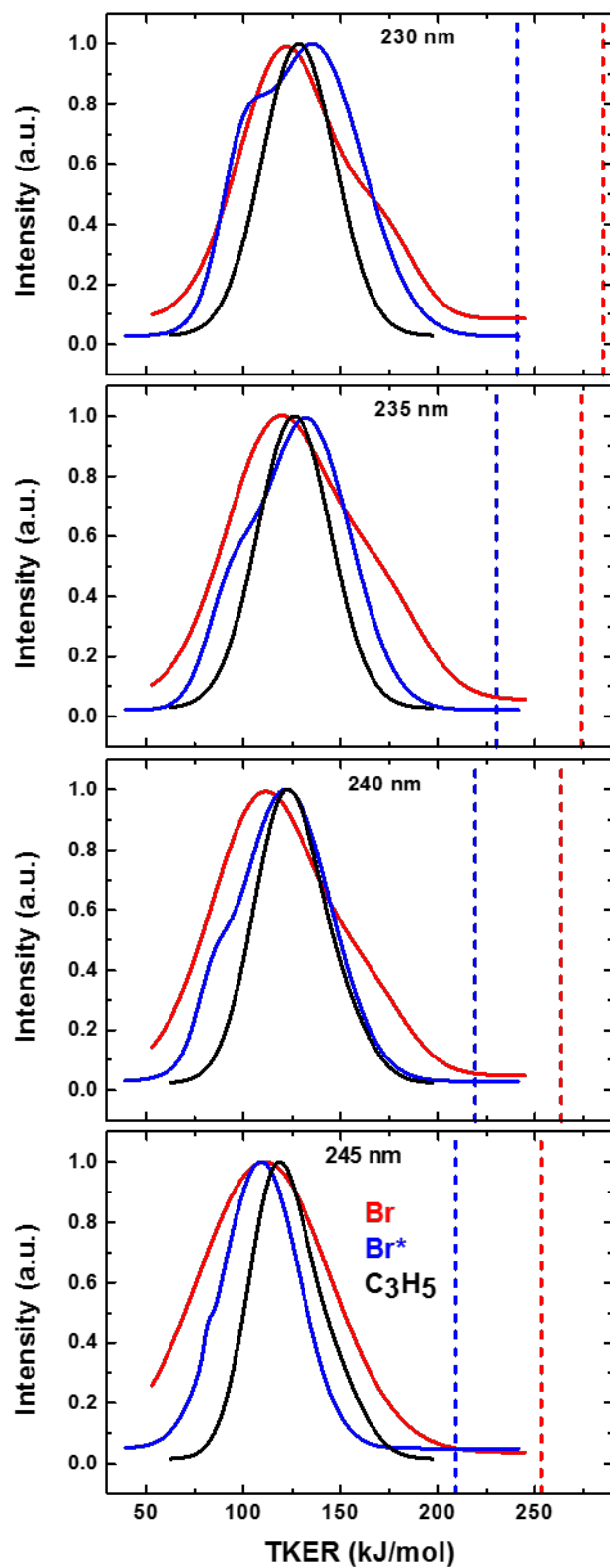


FIG. 6. Total kinetic energy release distributions deduced from analysis of the different photofragments from allyl bromide at four different photolysis wavelengths. The red curve is from analysis of Br ($^2P_{3/2}$) images, the blue curve from Br* ($^2P_{1/2}$) images, and the black curve from C₃H₅ fragment images. The vertical dashed lines represent the thermodynamic limits for the Br (red) or Br* (blue) and allyl radicals (with no internal energy) channel.

Figure 7 compares the TKER distributions deduced from hydrocarbon radical images obtained from photolysis of allyl bromide and bromocyclopropane. The distributions for these two hydrocarbon radical fragments are similar, but not identical to one another. The same is true for the photofragment anisotropies (see Tables III and VII). We conclude that the hydrocarbon radicals observed as a minor pathway in bromocyclopropane photolysis, and assigned as allyl fragments, are not the result of a small amount of allyl bromide contamination. In spite of differences in C-Br bond dissociation energies for the two molecules, the similarities in TKER distributions and recoil velocity anisotropies point towards common intermediate structures and dissociation products. This observation is in accord with the deductions of Carpenter and co-workers from their photodissociation experiments on iodocyclopropane.²⁷ The average TKERs in BCP are consistently lower than AB at all photolysis wavelengths, which can be accounted for by the greater structural change from Cp to allyl radical channelling more internal energy into the allyl fragment. This internal excitation is consistent with an apparently unstructured REMPI spectrum for our allyl photofragments.

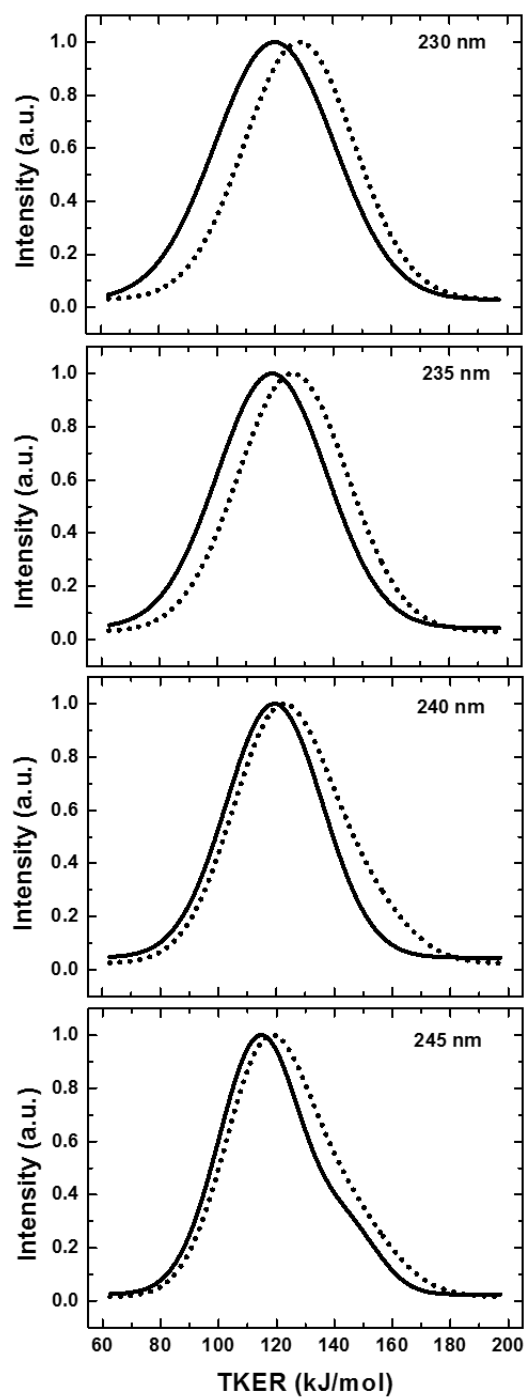


FIG. 7. Total kinetic energy release distributions deduced from analysis of the C_3H_5 photofragments from bromocyclopropane (solid line) and allyl bromide (dotted line) at four different photolysis wavelengths.

C. Velocity-map imaging of photofragments from bromocyclopropane cation and allyl bromide cation

Our hypothesis of concerted ring opening of photoexcited bromocyclopropane to give $Br/Br^* +$ allyl radical products is predicated on interpretation of TKER distributions and anisotropy parameter values that we attribute to dissociation of neutral

molecules. We therefore need to confirm that photolysis of the molecular cations does not result in comparable outcomes that contaminate the higher speed components of the images reported in Figure 3. In Sections **III.A** and **III.B**, we suggested that photolysis of the cations of the parent molecules is responsible for the low TKER components seen in images obtained from detection of $m/z = 41$ products. This section presents further evidence in support of this assignment, and shows that the faster $C_3H_5^+$ signals are unlikely to result from cation photolysis.

Table VIII summarizes energy values relevant to the discussion of the cation photodissociation. In Section III.B, we proposed that the low TKER components of $m/z = 41$ images from allyl bromide photolysis derived from the AB^+ cation, based in part on the observed onset at a wavelength near 235 nm. The ionization energy of BCP lies in the range 926-958 kJ mol⁻¹ (Table VIII), which is lower than that of allyl bromide, and the two-photon ionization threshold for BCP therefore lies within the wavelength range between 250 nm and 258 nm. This longer threshold wavelength results in the observed signatures of cation photodissociation as a slow central component in all the $m/z = 41$ images from BCP shown in Figure 3. The low-TKER distributions are similar to those reported in prior observations of the photodissociation of cations of alkyl halides.^{10,58} The energy provided by two photons at wavelengths down to 235 nm is not sufficient both to ionize and dissociate either molecule, so absorption of a third photon is necessary to induce cation photodissociation. The two-photon ionization at energies just above threshold will produce the ground electronic state of the cation with low internal energy, from which photolysis proceeds.

The threshold energies for $C_3H_5Br^+$ cation (with $C_3H_5 = Cp$ or allyl) dissociation to $C_3H_5^+ + Br/Br^*$ or $C_3H_5 + Br^+$ are compared in Table VIII. In the case of bromocyclopropane, the ground state of BCP^+ is bound by only ~200 kJ mol⁻¹ with respect to $Cp^+ + Br$, and a further photon of wavelength 230 – 245 nm is sufficient to induce this dissociation. This mechanism accounts for our observation of signatures of the cation photolysis in our $m/z = 41$ images. However, $\lambda = 230 - 245$ nm photons are not energetic enough to generate excited state BCP^+ with the 550 kJ mol⁻¹ of energy needed to dissociate to $C_3H_5 + Br^+$, which indicates why we do not observe slow Br^+ from cation photolysis in our images for Br and Br^* products. The energy ordering of the dissociation limits does not fully explain the absence of cation photodissociation signals in the Br/Br^* images, because the two-colour experiments involved a probe laser tuned to Br or Br^* REMPI transitions. Hence neutral Br/Br^* fragments from the cation dissociation might still be detected. Their absence suggests either signals much weaker than the Br/Br^* from the neutral parent photolysis (recall that we used low photolysis laser pulse energies in the experiments probing Br/Br^* , which bias against cation formation), or cation fragmentation pathways that do not favour bromine atom or ion production.

Table VIII: Reaction enthalpies of different dissociation channels for BCP⁺ and AB⁺.

Molecule	Ionization energy (kJ mol ⁻¹)	Dissociation process	Reaction enthalpy (kJ mol ⁻¹) ^b
Bromocyclopropane (BCP)	926-958 ($\lambda = 258 - 250$ nm) ^a	BCP ⁺ \rightarrow Cp ⁺ + Br	202
		BCP ⁺ \rightarrow Cp ⁺ + Br [*]	246
		BCP ⁺ \rightarrow Cp + Br ⁺	551
Allyl bromide (AB)	964-982 ($\lambda = 248 - 244$ nm) ^a	AB ⁺ \rightarrow Allyl ⁺ + Br	57
		AB ⁺ \rightarrow Allyl ⁺ + Br [*]	101

^aThreshold wavelength for 2-photon ionization.^bTo calculate reaction enthalpy, we used the ionization energies of AB and allyl radical⁵³ for AB⁺ + Br/Br^{*} and the ionization energies of BCP and cyclopropyl radical⁵⁴ for BCP⁺ + Br/Br^{*}.

We studied the pathways open to BCP⁺ or AB⁺ photolysis, and the TKERs of the resulting photofragments, using 118-nm single-photon ionization of the neutral parent molecule to prepare ground state molecular cations. This wavelength corresponds to a photon energy of 1011 kJ mol⁻¹, which is sufficient to ionize either parent molecule to form the ground electronic state of the cation, but not to access asymptotes for cation dissociation. The 118-nm VUV laser beam contained residual 355-nm radiation (with photon energy of 337 kJ mol⁻¹) which brought about photodissociation of the molecular cations, and we imaged the resulting $m/z = 41$ C₃H₅⁺ products. A small amount of $m/z = 39$ (C₃H₃⁺) was also observed in the TOF mass spectra, as well as $m/z = 120$ and 122 (BCP⁺).

In further experiments using two lasers, pulses of a second wavelength in the range 230 - 240 nm were temporally and spatially overlapped with the 118/355 nm pulses inside the imaging chamber to dissociate BCP⁺. The presence of this additional UV wavelength significantly reduced the $m/z=122$, 120 and 41 signals, with $m/z=40$ (C₃H₄⁺), $m/z=39$ (C₃H₃⁺) and $m/z=38$ (C₃H₂⁺) observed to be major products. Vallance and co-workers¹⁰ reported similar behaviour in their studies of C₂H₅Br⁺ and C₂H₅I⁺ photolysis.

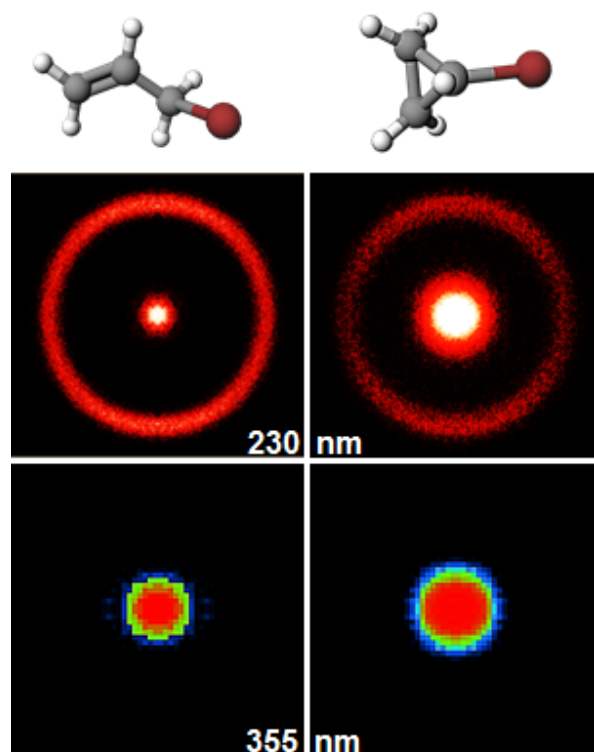


FIG. 8. Velocity map images of $m/z = 41$ photofragments from allyl bromide (left column) and bromocyclopropane (right column). Top row: photoexcitation and dissociation of neutral parent molecules at 230 nm. Bottom row: photodissociation of AB^+ and BCP^+ at 355 nm. Images in the top row were recorded using a CCD camera, and in the bottom row using a lower resolution PImMS camera.

Figure 8 shows velocity map images obtained at $m/z=41$ after BCP^+ and AB^+ photolysis at 355 nm, together with the deduced TKER distribution for the photofragments. These are compared with the images obtained by photolysis of neutral BCP and AB, which highlights the similarities in the slow-moving fragment distributions seen in the two sets of experiments. The fractions of total available energy entering translational degrees of freedom of the photofragments from the cationic species are summarized in Table IX, and the derived TKER distributions are shown in Supplemental Material.³¹ For both molecular cations, we observe only slow dissociation products, with no rings in the images from fast photofragments. The introduction of 230-240 nm photons does not produce any such additional rings for images accumulated at $m/z = 41$. The TKER is only ~4% of the total available energy, which is comparable to prior reports of alkyl halide cation photodissociation dynamics,¹⁰ and to the low TKER components seen in Figs. 3 and 5, but significantly smaller than for the TKERs we assign to neutral molecule dissociation pathways in Sections III.A and III.B. The 118-nm ionization experiments therefore support our arguments that the slow-moving hydrocarbon radical fragments are not associated with neutral parent molecule dissociation pathways, but instead result from cation photolysis, whereas all other observed signals are from neutral dissociation mechanisms.

TABLE IX: Total available energies, most probable total kinetic energy release values, and fractions of the total available energy in translation for $m/z = 41$ fragments and coincidentally produced Br or Br* atoms after UV photolysis of BCP⁺ and AB⁺.

Parent ion	Total Available Energy (kJ mol ⁻¹)				TKER (kJ mol ⁻¹)		$\langle f_i \rangle$
	355 nm		230 nm		355 nm	230 nm ^a	
	Br	Br*	Br	Br*	C ₃ H ₅ ⁺	C ₃ H ₅ ⁺	
BCP ⁺	135.0	91.0	318.1	274.1	8.1	19.0	0.06
AB ⁺	280.3	236.3	463.4	419.4	5.3	8.8	0.02

^aThe TKERs for 230 nm photolysis are estimated by assuming the fraction of total available energy that enters translation is the same as at 355 nm.

D. Summary of the photodissociation pathways observed in bromocyclopropane and allyl bromide

One-photon UV excitation of bromocyclopropane and the ensuing dissociation produces both Br and Br* fragments with narrow distributions of kinetic energy, despite the many degrees of vibrational and rotational freedom accessible to the radical co-product. The peaks of these kinetic energy distributions scale linearly with photon energy, and the distributions lie within the expected thermodynamic limits for simple C-Br bond cleavage. The anisotropies of the photofragment velocity distributions show that the dominant excitation in the parent molecule is to the ³Q₀ state, and that a conical intersection with the ¹Q₁ state influences the photodissociation dynamics, which occur promptly on one or more repulsive PESs.

C₃H₅ radicals resulting from BCP photolysis, and detected by ionization at 230 – 245 nm, show higher kinetic energy release than is deduced from analysis of the Br and Br* fragments. Spatial anisotropy of the C₃H₅ fragment images is lower than observed in corresponding Br and Br* images. We conclude that a minor pathway involves concerted C-Br bond cleavage and opening of the cyclopropyl ring to form the lower-energy allyl radical, providing additional energy to the photofragments, of which <20% enters translational motion. A similar pathway has been proposed in iodocyclopropane, and is argued to be mediated by a PES corresponding to an ion-pair state with C₃H₅⁺I⁻ character, in which the cationic nature of the cyclopropyl moiety promotes spontaneous ring-opening.²⁷ Two non-adiabatic transitions are required, first onto the ion pair state and then back to a repulsive valence state after the cyclopropyl ring has opened. This mechanism circumvents the high barrier to the ring-opening isomerization on the PES(s) with valence character. Alternative assignments of the C₃H₅⁺ signals, for example to photolysis of the BCP⁺ cation accidentally prepared by multiphoton ionization of BCP by the photolysis laser, are discounted on the basis of further measurements which include imaging the photodissociation of BCP⁺ prepared by 118-nm ionization.

We now consider possible pathways for ring-opening and C-Br bond fission in photoexcited BCP in greater detail. Our REMPI scheme around 240 nm probes neutral allyl radicals resonantly,⁵⁹ and no study of which we are aware reports comparable sensitivity to cyclopropyl radicals. We therefore assume that images obtained with this detection method reveal the velocities of allyl radicals, and not cyclopropyl radicals, regardless of whether the precursor molecule is BCP or AB. This assumption is supported by the measured TKER distributions and photofragment velocity anisotropies. The images also feature contributions from ions of mass 41 produced by other pathways, which include photolysis of BCP⁺ cations to make Br + C₃H₅⁺ fragments. Starting from BCP, the routes we consider to explain the contributions to the $m/z = 41$ images are: (1) concerted ring-opening of the cyclopropyl ring and dissociation of the Br bond, perhaps via a pathway mediated by an ion-pair state with barrierless ring-opening,²⁷ as described above; (2) prompt bond dissociation to Br + cyclopropyl radical, with subsequent ring-opening of the fraction of cyclopropyl radicals formed with sufficient internal energy to surmount the 79-88 kJ mol⁻¹ barrier to isomerization to allyl radical; (3) isomerization of the one-photon excited BCP to internally excited AB*, and subsequent photolysis of this AB* by a second photon from the photolysis laser; (4) photolysis of BCP⁺ via its lowest energy asymptote, Br + C₃H₅⁺, with the direct imaging of the $m/z = 41$ ion preventing our discriminating between allyl⁺ and cyclopropyl⁺.

We have argued above that pathway (4) only accounts for the slow C₃H₅⁺ photoproducts seen as central features in our velocity map images, and concentrate on pathways (1) – (3) involving neutral photochemistry in considering the faster rings in the images in Figure 3. Figure 9 summarizes pathways (1) – (3), leading to neutral allyl radicals, and the associated features of the images we expect to see for $m/z = 41$ ions after 1+1 ionization.

The mechanism proposed in pathway (1) (purple in Figure 9), namely unimolecular dissociation of UV-excited BCP via an ion-pair state, giving concerted C-Br fission and cyclopropyl to allyl isomerization, is the only one that plausibly accounts for all of our experimental observations. However, it must be a minor channel in BCP photolysis because it does not leave clear signatures on the TKER distributions deduced from analysis of Br and Br* images and shown in Figure 4. The majority of the photoexcited BCP molecules undergo direct C-Br bond fission, while retaining the Cp ring, and dominate these TKER distributions.

Isomerization of internally excited Cp photofragments (pathway (2); blue in Figure 9) would favour low C₃H₅ fragment speeds and low TKERs because ≥ 79 kJ mol⁻¹ of the available ≤ 182.5 kJ mol⁻¹ must have entered internal modes of the Cp radicals to overcome the isomerization barrier to allyl radicals. This pathway can therefore be discounted on the evidence of TKER distributions obtained from our images and shown in Figure 7.

Isomerization of photoexcited BCP to AB* is a first step in both pathways (1) and (3). Secondary photolysis of AB* (pathway (3); green in Figure 9) might give images similar to those obtained by photodissociation of ground-state AB, but these

are likely to extend to significantly greater TKER because two photons have been absorbed. The images would also be expected to show broader speed distributions reflecting the distribution of internal energy of the AB^* molecules over many modes. We observe that the peaks and widths of the TKER distributions deduced from images for $m/z = 41$ and Br/Br^* fragments from BCP and AB are similar (Figs. 7 and S.7). Furthermore, the peaks of the TKER distributions from allyl bromide photolysis scale linearly with photolysis laser energy, whereas the hydrocarbon radical fragments imaged from BCP photolysis peak at the same translational energy irrespective of dissociative photon energy (Supplemental Material,³¹ Figure S.7). This evidence argues against secondary photolysis of AB^* as the source of the observed allyl radicals from BCP photolysis. Regardless, any contribution from this pathway still requires ring-opening of the photoexcited BCP to compete with direct C-Br bond fission.

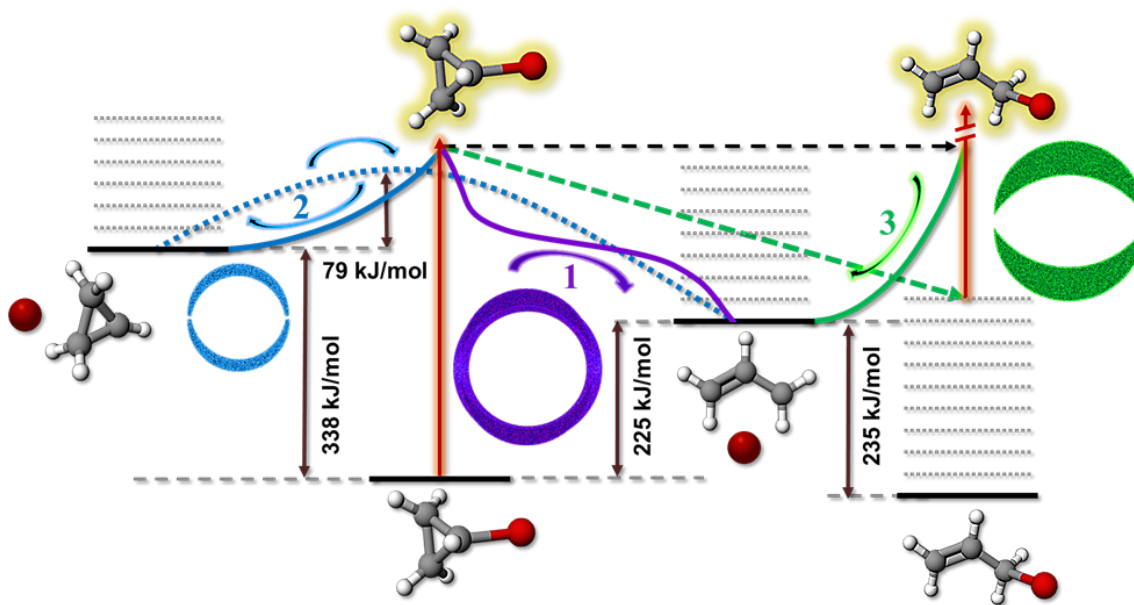


FIG. 9. Proposed mechanisms for the formation of ring-opened allyl radicals from photodissociation of bromocyclopropane, with sketches of predicted velocity-map images for $m/z = 41$ photofragments. Vertical red lines represent the photo-excitation of BCP and AB. UV excited BCP^* mostly dissociates into Cp and Br/Br^* via repulsive PESs along the C-Br coordinate (pathway 2, solid blue line). Cp radicals with more than 79 kJ mol^{-1} of internal energy can isomerize over a barrier (dotted blue line) to allyl radicals, and the expected velocity map image is sketched in blue. In pathway 1 (solid purple line), concerted ring-opening of the cyclopropyl ring and dissociation of the C-Br bond occur via an ion-pair state that intersects the repulsive valence states at two points along the reaction pathway (see ref. 27). A sketch of the expected image for allyl fragments is shown in purple. If BCP^* isomerizes to vibrationally excited AB^* (dotted green line), photolysis by absorption of a second photon will produce fast and vibrationally excited allyl radicals with a broad speed distribution (pathway 3). A schematic image is shown in green.

IV. CONCLUSIONS:

Photodissociation of bromocyclopropane in its A-band at wavelengths in the range 230 – 267 nm produces both ground-state and spin-orbit excited bromine atoms, and the majority of the co-products are cyclopropyl radicals. However, a

minor pathway involves concerted C-Br bond fission and opening of the cyclopropyl ring, forming a lower energy allyl radical in partnership with the Br or Br* and releasing additional energy for product translation. Complementary studies of the photodissociation of isomeric allyl bromide indicate that minor impurities of this compound in the bromocyclopropane sample are not responsible for the observed allyl radicals. We estimate that fewer than 5% of dissociations of photoexcited bromocyclopropane follow the concerted ring-opening and C-Br fission pathway at the chosen UV wavelengths. Isomerization of the cyclopropyl moiety to an allyl group on the directly photoexcited valence state or the ground state PES is hampered by a high activation barrier and is unlikely to compete effectively with the direct C-Br bond fission to Br + cyclopropyl radical products. An alternative pathway involving crossing to an ion-pair state, previously proposed to occur in iodocyclopropane dissociation, may also be active in bromocyclopropane; cationic character in the cyclopropyl ring of the Cp^+X^- ion pair state ($\text{X} = \text{Br}$ or I) facilitates isomerization to an allyl cation with a much reduced energy barrier. A second crossing is then required to return from the ion-pair state to the repulsive valence state of allyl bromide.

The minor ring-opening pathway is not easily discernible from images of the Br and Br* products alone, but is revealed by comparison of TKER distributions deduced from analysis of images obtained for both the bromine atom and the C_3H_5 radical co-fragment. 1+1 REMPI at wavelengths around 230 nm selectively probes the allyl product over cyclopropyl radical fragments in images collected for $m/z = 41$. Momentum-matching arguments often make it unnecessary to image the velocities of both products of a photodissociation, however, this study illustrates that comparison of TKER distributions for both photoproducts can reveal unusual dynamical pathways.

ACKNOWLEDGEMENTS

We thank EPSRC for funding this work in both the Bristol and Oxford groups through Programme Grant EP/L005913/1. S.P. acknowledges the University of Bristol for award of a postgraduate scholarship. We thank B.K. Carpenter and M.N.R. Ashfold for valuable discussions.

Supplemental Material

The Supplemental Material contains: analysis of sample purities; velocity map images of Br and Br* from UV photolysis of allyl bromide and their analysis; a comparison of TKER distributions for Br and Br* from bromocyclopropane photolysis; a comparison of the anisotropy parameters and TKER distributions for the C_3H_5 products from bromocyclopropane and allyl bromide photolysis; a comparison of the TKER distributions derived from images for photolysis of the molecular cations of allyl bromide and bromocyclopropane.

All experimental data are archived in the University of Bristol's Research Data Storage Facility (DOI 10.5523/bris.te9ou22hm25v18e1b9ia5wbyl).

REFERENCES

- ¹ Y.L. Yung, J.P. Pinto, R.J. Watson, and S.P. Sander, *J. Atmos. Sci.* **37**, 339 (1980).
- ² R.P. Wayne, *The Chemistry of Atmospheres*, 2nd ed. (Oxford University Press, New York, 1991).
- ³ S.C. Wofsy, M.B. McElroy, and Y. I. Yung, *Geophys. Res. Lett.* **2**, 215 (1975).
- ⁴ “*Methyl Bromide: Its Atmospheric Science, Technology, and Economics*,” (United Nations Environment Program, Nairobi, Kenya, 1992).
- ⁵ T. Gougousi, P.C. Samartzis, and T.N. Kitsopoulos, *J. Chem. Phys.* **108**, 5742 (1998).
- ⁶ R. Zhu, B. Tang, X. Zhang, and B. Zhang, *J. Phys. Chem. A* **114**, 6188 (2010).
- ⁷ B. Tang and B. Zhang, *Chem. Phys. Lett.* **412**, 145 (2005).
- ⁸ Y. Wang, S. Zhang, Z. Wei, Q. Zheng, and B. Zhang, *J. Chem. Phys.* **125**, 184307 (2006).
- ⁹ J.G. Underwood and I. Powis, *Phys. Chem. Chem. Phys.* **2**, 747 (2000).
- ¹⁰ S.H. Gardiner, T.N. V Karsili, M.L. Lipciuc, E. Wilman, M.N.R. Ashfold, and C. Vallance, *Phys. Chem. Chem. Phys.* **16**, 2167 (2014).
- ¹¹ R.S. Mulliken, *J. Chem. Phys.* **8**, 382 (1940).
- ¹² D. Murdock, S.J. Harris, J. Luke, M.P. Grubb, A.J. Orr-Ewing, and M.N.R. Ashfold, *Phys. Chem. Chem. Phys.* **16**, 21271 (2014).
- ¹³ X. Qian, *J. Phys. Chem. B* **117**, 11460 (2013).
- ¹⁴ M. Saab, L.J. Doriol, B. Lasorne, S. Guérin, and F. Gatti, *Chem. Phys.* **442**, 93 (2014).
- ¹⁵ G. Szeimies and G. Boche, *Angew. Chemie Int. Ed. English* **10**, 912 (1971).
- ¹⁶ P.A. Arnold and B.K. Carpenter, *Chem. Phys. Lett.* **328**, 90 (2000).
- ¹⁷ S. Olivella, A. Sole, and J.M. Bofill, *J. Am. Chem. Soc.* **112**, 2160 (1990).

- ¹⁸ D.J. Mann and W.L. Hase, J. Am. Chem. Soc. **124**, 3208 (2002).
- ¹⁹ J.M. Hostettler, L. Castiglioni, A. Bach, and P. Chen, Phys. Chem. Chem. Phys. **11**, 8262 (2009).
- ²⁰ O.N. Faza, C.S. López, R. Alvarez, and A.R. de Lera, J. Org. Chem. **69**, 9002 (2004).
- ²¹ Z.C. Kramer, B.K. Carpenter, G.S. Ezra, and S. Wiggins, J. Phys. Chem. A **119**, 6611 (2015).
- ²² G. Greig and J.C.J. Thynne, Trans. Faraday Soc. **62**, 3338 (1966).
- ²³ G. Greig and J.C.J. Thynne, Trans. Faraday Soc. **63**, 1369 (1967).
- ²⁴ J.A. Kerr, A. Smith, and A.F. Trotman-Dickenson, J. Chem. Soc. A Inorganic, Phys. Theor. 1400 (1969).
- ²⁵ D.J. DeFrees, R.T. McIver, and W.J. Hehre, J. Am. Chem. Soc. **102**, 3334 (1980).
- ²⁶ J. Berkowitz, G.B. Ellison, and D. Gutman, J. Phys. Chem. **98**, 2744 (1994).
- ²⁷ P.A. Arnold, B.R. Cosofret, S.M. Dylewski, P.L. Houston, and B.K. Carpenter, J. Phys. Chem. A **105**, 1693 (2001).
- ²⁸ X. Zheng, C.W. Lee, and D.L. Phillips, Chem. Phys. Lett. **366**, 656 (2002).
- ²⁹ P.J. Kropp, Acc. Chem. Res. **17**, 131 (1984).
- ³⁰ R.A. Rose, S.J. Greaves, and A.J. Orr-Ewing, J. Chem. Phys. **132**, 244312 (2010).
- ³¹ *No Title* (n.d.).
- ³² D.H. Parker and A.T.J.B. Eppink, J. Chem. Phys. **107**, 2357 (1997).
- ³³ W.S. Hopkins, M.L. Lipciuc, S.H. Gardiner, and C. Vallance, J. Chem. Phys. **135**, 034308 (2011).
- ³⁴ A.T. Clark, J.P. Crooks, I. Sedgwick, R. Turchetta, J.W.L. Lee, J.J. John, E.S. Wilman, L. Hill, E. Halford, C.S. Slater, B. Winter, W.H. Yuen, S.H. Gardiner, M.L. Lipciuc, M. Brouard, A. Nomerotski, and C. Vallance, J. Phys. Chem. A **116**, 10897 (2012).
- ³⁵ K. Amini, S. Blake, M. Brouard, M.B. Burt, E. Halford, A. Lauer, C.S. Slater, J.W.L. Lee, and C. Vallance, Rev. Sci. Instrum. **86**, 103113 (2015).
- ³⁶ A. V Komissarov, M.P. Minitti, A.G. Suits, and G.E. Hall, J. Chem. Phys. **124**, 14303 (2006).
- ³⁷ R.N. Zare and D.R. Herschbach, Bull. Am. Phys. Soc. **7**, 458 (1962).
- ³⁸ R.S. Mulliken, J. Chem. Phys. **3**, 573 (1935).

- ³⁹ D. Porret and C.F. Goodeve, *Trans. Faraday Soc.* **33**, 690 (1937).
- ⁴⁰ T.F. Hunter and K.S. Kristjansson, *Chem. Phys. Lett.* **58**, 291 (1978).
- ⁴¹ Y. Zhao and D.G. Truhlar, *Theor. Chem. Acc.* **120**, 215 (2007).
- ⁴² T.H. Dunning, *J. Chem. Phys.* **90**, 1007 (1989).
- ⁴³ A.S. Bracker, E.R. Wouters, A.G. Suits, and O.S. Vasyutinskii, *J. Chem. Phys.* **110**, 6749 (1999).
- ⁴⁴ L. Landau, *Phys. Zeitschrift Der Sowjetunion* **2**, 46 (1932).
- ⁴⁵ C. Zener, *Proc. R. Soc. A* **137**, 696 (1932).
- ⁴⁶ R.A. Seburg and R.R. Squires, *Int. J. Mass Spectrom. Ion Process.* **167-168**, 541 (1997).
- ⁴⁷ M.W. Chase, *NIST-JANAF Thermochemical Tables*, Fourth Edi (J. Phys. Chem. Ref. Data, Monograph 9, 1998).
- ⁴⁸ R. Schinke, *Photodissociation Dynamics* (Cambridge University Press, Cambridge, 1993).
- ⁴⁹ W.S. McGivern, R. Li, P. Zou, and S.W. North, *J. Chem. Phys.* **111**, 5771 (1999).
- ⁵⁰ W.P. Hess, D.W. Chandler, and J.W. Thoman, *Chem. Phys.* **163**, 277 (1992).
- ⁵¹ Y. Amatatsu, K. Morokuma, and S. Yabushita, *J. Chem. Phys.* **94**, 4858 (1991).
- ⁵² Y. Amatatsu, S. Yabushita, and K. Morokuma, *J. Chem. Phys.* **104**, 9783 (1996).
- ⁵³ N.D. Kagramanov, K. Ujszaszy, J. Tamas, A.K. Mal'tsev, and O.M. Nefedov, *Bull. Acad. Sci. USSR Div. Chem. Sci.* **32**, 1531 (1983).
- ⁵⁴ J. Dyke, A. Ellis, N. Jonathan, and A. Morris, *J. Chem. Soc. Faraday Trans. 2* **81**, 1573 (1985).
- ⁵⁵ L. Ji, Y. Tang, R. Zhu, Z. Wei, and B. Zhang, *J. Chem. Phys.* **125**, 164307 (2006).
- ⁵⁶ J.C. Traeger, *Int. J. Mass Spectrom. Ion Process.* **58**, 259 (1984).
- ⁵⁷ H. Schmidt and A. Schweig, *Angew. Chemie Int. Ed. English* **12**, 307 (1973).
- ⁵⁸ P.C. Samartzis, B.L.G. Bakker, D.H. Parker, and T.N. Kitsopoulos, *J. Phys. Chem. A* **103**, 6106 (1999).
- ⁵⁹ D.W. Minsek, J.A. Blush, and P. Chen, *J. Phys. Chem.* **96**, 2025 (1992).

Supplemental Material: Evidence for Concerted Ring Opening and C-Br Bond Breaking in UV-Excited Bromocyclopropane

Shubhrangshu Pandit,¹ Thomas J. Preston,^{1,b)} Simon J. King,² Claire Vallance² and Andrew J. Orr-Ewing^{1,a)}

(1) School of Chemistry, University of Bristol, Cantock's Close, Bristol, BS8 1TS, UK.

(2) Department of Chemistry, University of Oxford, Chemistry Research Laboratory, 12 Mansfield Road, Oxford OX1 3TA, UK

S.1. Sample Purity

FTIR spectra (recorded in a PerkinElmer Spectrum Two LiTa FTIR Spectrometer) of allyl bromide (AB) and bromocyclopropane (BCP) vapour are presented in Figure S.1. This spectroscopic analysis was carried out to check the purity of the commercial samples. The C=C stretching vibrational mode of allyl bromide at around 1680 cm^{-1} is missing in the bromocyclopropane spectrum, which confirms that AB is not a significant impurity (at most 3% based on the signal-to-noise levels in the FTIR spectra) in the BCP samples.

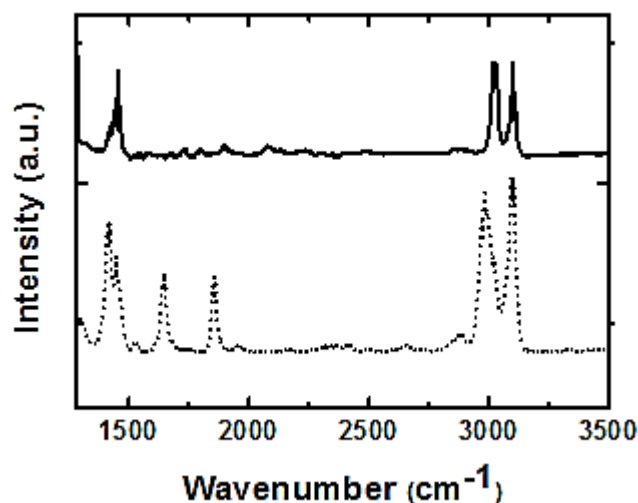


FIG. S.1. FTIR spectra of gaseous samples of allyl bromide (dotted line) and bromocyclopropane (solid line).

^{a)} Author for correspondence: a.orr-ewing@bristol.ac.uk

^{b)} Current address: Institute for Energy Technology, Instituttveien 18, NO-2007 Kjeller, Norway

S.2. Br and Br* images and derived TKER distributions from UV photolysis of allyl bromide

The photodissociation of allyl bromide at wavelengths spanning 230 – 245 nm was studied, in part to test whether contamination of allyl bromide in the bromocyclopropane sample arose through BCP sample degradation in our gas handling systems. Velocity-map images obtained by REMPI detection of Br and Br* fragments are shown in Figure S.2. The images reveal two overlapping components, which are more readily discerned when the speed distributions are converted to total kinetic energy release (TKER) distributions of the photofragments. These distributions are shown in Figure S.3. The difference in TKER distribution maxima for the two processes amounts to $\sim 50 \text{ kJ mol}^{-1}$ for Br fragments and $\sim 40 \text{ kJ mol}^{-1}$ for Br* fragments. This difference is greater than the energy differences of torsional isomers of allyl bromide. The fractions of total available energy entering translational motions of the photofragments, $\langle f_t \rangle$, are presented in Table S.1. The $\langle f_t \rangle$ values of all the photofragments from allyl bromide are lower than those for the photofragments from bromocyclopropane at all photolysis wavelengths. The slower component of the Br images is more intense than the faster component, and the reverse is true in Br* images. In both cases, the stronger component in the images gives rise to a narrower TKER distribution than the weaker component. These observations suggest either contributions from a different channel than dissociation directly via the A-band excited states,⁵³ or different degrees of vibrational excitation in the companion allyl radical. This bimodal nature of TKER is consistent with the work by Ji *et al.*⁵³ and they have provided an interpretation of the photochemistry.

TABLE S.I. Fraction of the total available energy entering the translational degrees of freedom of photofragments of allyl bromide at four different photolysis wavelengths. Where two values are specified, they correspond to the slower and faster components of the bimodal TKER distribution.

Allyl bromide photofragments	$\langle f_t \rangle^a$			
	230 nm	235 nm	240 nm	245 nm
Br + allyl	0.42/0.60	0.43/0.62	0.42/0.62	0.43
Br* + allyl	0.41/0.56	0.40/0.58	0.38/0.55	0.39/0.52

^a Uncertainties in $\langle f_t \rangle$ are $< 2\%$ for both Br and Br* fragments at all photolysis wavelengths.

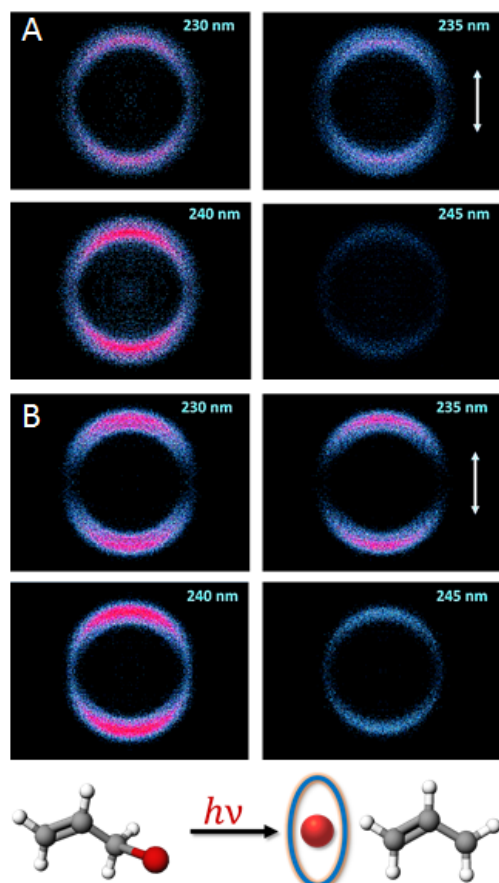


FIG. S.2. Time-sliced velocity map images of (A) Br ($^2P_{3/2}$) and (B) Br ($^2P_{1/2}$) photofragments from allyl bromide at four different photolysis wavelengths. The photolysis laser polarisation vector is oriented parallel to the vertical axis of these images, as shown by the double-headed white arrows in two panels. Signal intensity at 245 nm was much reduced and only a single component is observed in the product speed distribution at this wavelength.

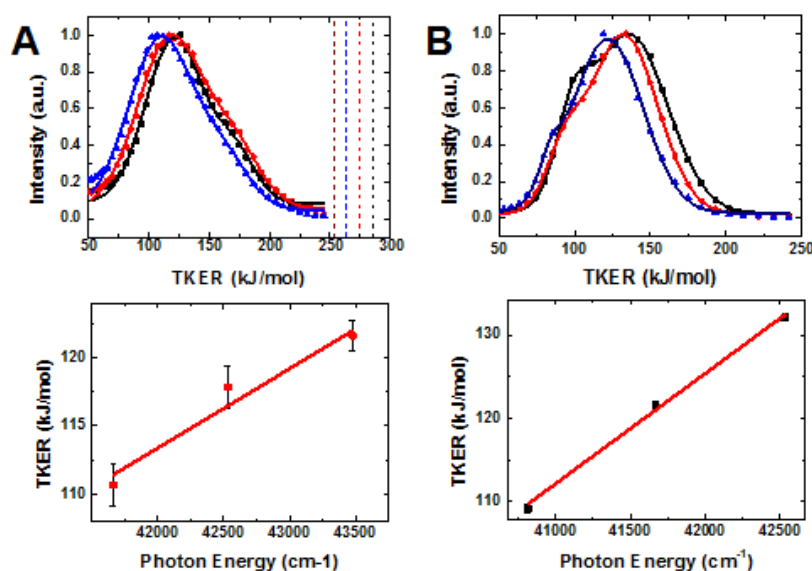


FIG. S.3. Total kinetic energy release distributions deduced from images of (A) Br and (B) Br* photofragments from allyl bromide at photolysis wavelengths of 230 nm (black), 235 nm (red), 240 nm (blue). Symbols are experimental data points and the solid lines are cumulative plots from double Gaussian fits. The vertical dashed lines in (A) represent the thermodynamic limits for production of Br ($^2P_{3/2}$) and allyl radical (with no internal energy) at these different wavelengths. The peaks (slow component for Br and fast component for Br*) of the total kinetic energy release distributions are plotted as a function of photolysis photon energy in the bottom panels with linear fits shown in red.

The TKER distributions for photofragments from allyl bromide are presented in Figure S.3. All the products have total kinetic energies within the expected thermodynamic limits for the Br + allyl dissociation pathway, and the maxima of the distributions scale linearly with UV photon energy.

The corresponding images obtained at $m/z = 41$ following UV photolysis of allyl bromide and the derived TKER distributions are shown in Figures 6 and 7 of the main manuscript.

S.3. Comparison of TKER distributions obtained for the Br and Br* channels from bromocyclopropane photolysis

The TKER distributions deduced from analysis of the images obtained for Br and Br* photofragments from BCP are presented in Figure S.4. The vertical lines represent the thermodynamic limits for the specific dissociation process at different excitation wavelengths, with the assumption that the co-fragment is a cyclopropyl radical. All the peaks fitted well to single Gaussian functions. The peaks of the TKER distributions scale linearly with UV photon energy.

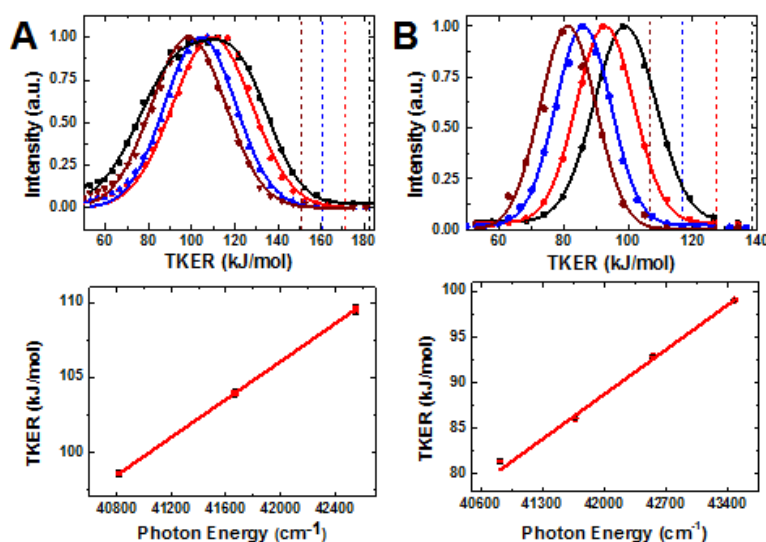


FIG. S.4. Total kinetic energy release distributions obtained from analysis of images for (A) Br and (B) Br* photofragments from bromocyclopropane at UV excitation wavelengths of 230 nm (black), 235 nm (red), 240 nm (blue) and 245 nm (wine). Symbols are experimental data points and the solid lines are Gaussian fits. The vertical dashed lines represent the thermodynamic limits for Br (${}^2P_{3/2}$) or Br* (${}^2P_{1/2}$) and Cp radicals at each wavelength. The peaks of the TKER distributions are plotted as a function of photolysis photon energy in the bottom panels, with linear fits shown in red.

The average kinetic energy of Br + C₃H₅ photofragments from BCP is only 20 kJ mol⁻¹ higher than that for Br* + C₃H₅ fragments, whereas the total available energy is 44 kJ mol⁻¹ higher for the Br channel. These values

indicate greater internal excitation of the hydrocarbon radical co-fragments when formed with Br atoms. The extent of radical excitation also controls the widths of the kinetic energy distributions, and these are compared in Figure S.5 for Br and Br* forming pathways. A broader kinetic energy distribution implies a greater spread of the internal energy of the hydrocarbon radical photofragments. Possible causes of these differences are discussed in the main manuscript.

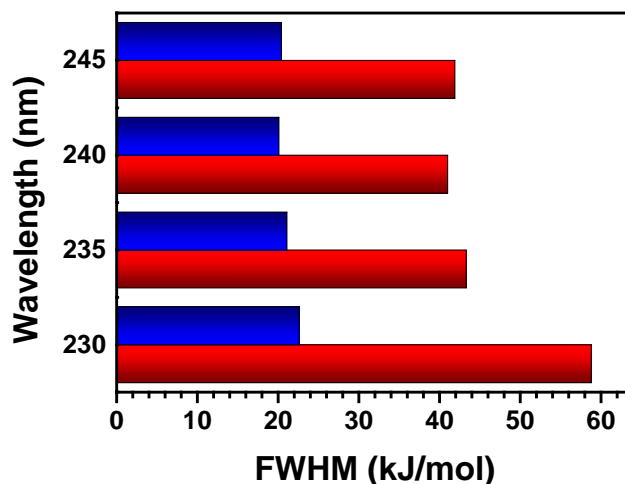


FIG. S.5. The FWHM of the TKER distributions derived from images for the Br (red) and Br* (blue) fragments from bromocyclopropane. The widths were obtained from Gaussian fits.

S.4. Comparison of anisotropy parameter values obtained for the C₃H₅ channels from bromocyclopropane and allyl bromide photolysis

The anisotropy parameters of allyl fragments from bromocyclopropane and allyl bromide averaged over all product speeds are similar but not identical. These small but systematic differences at all the photolysis wavelengths suggest a common radical photofragment produced from similarly structured intermediates.

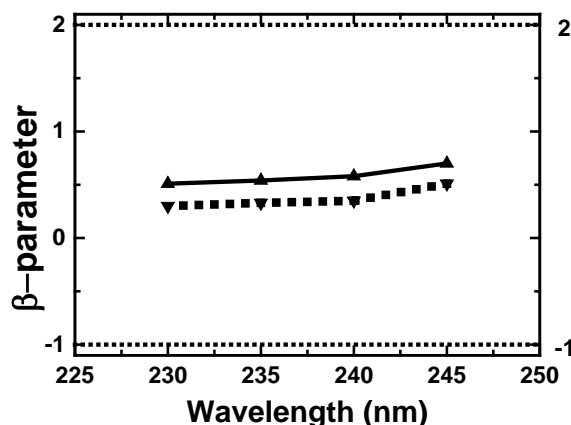


FIG. S. 6. Anisotropy parameters of C_3H_5 fragments from bromocyclopropane (solid line) and allyl bromide (dotted line). The anisotropy parameters are averaged over all photoproduct speeds in the outer rings seen in the velocity map images. Two horizontal dotted lines represent the two limiting values of the β -parameter (+2 for a parallel transition and -1 for a perpendicular transition).

S.5. Comparison of TKER distributions obtained for the C_3H_5 channels from bromocyclopropane and allyl bromide photolysis

As shown in Figure S. 7(A), the widths of the TKER distributions deduced from images for $m/z=41$ fragments from BCP and AB are very similar. The peaks of these TKER distributions are plotted in Figure S. 7 (B); the peak positions vary linearly with photolysis photon energy for AB, but are insensitive to the dissociative photon energy for BCP. This evidence argues against any contribution to our BCP $m/z = 41$ images from the secondary photolysis of AB^* (see section III.D of the main text).

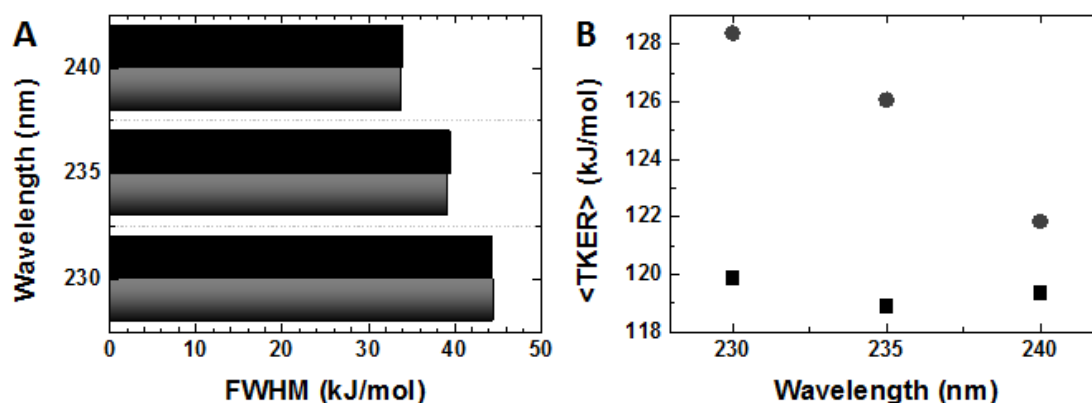


FIG. S. 7. (A) The FWHMs of the TKER distributions derived from C_3H_5 images for BCP (black) and AB (grey) at different photolysis wavelengths. The widths were obtained by Gaussian fits. (B) The peaks of the TKER distributions obtained from C_3H_5 photofragment images from BCP (black squares) and AB (grey circle) photolysis at three photolysis wavelengths.

S.6. Comparison of TKER distributions obtained from images for BCP⁺ and AB⁺ photolysis with the low TKER components from 230 nm photolysis of BCP and AB

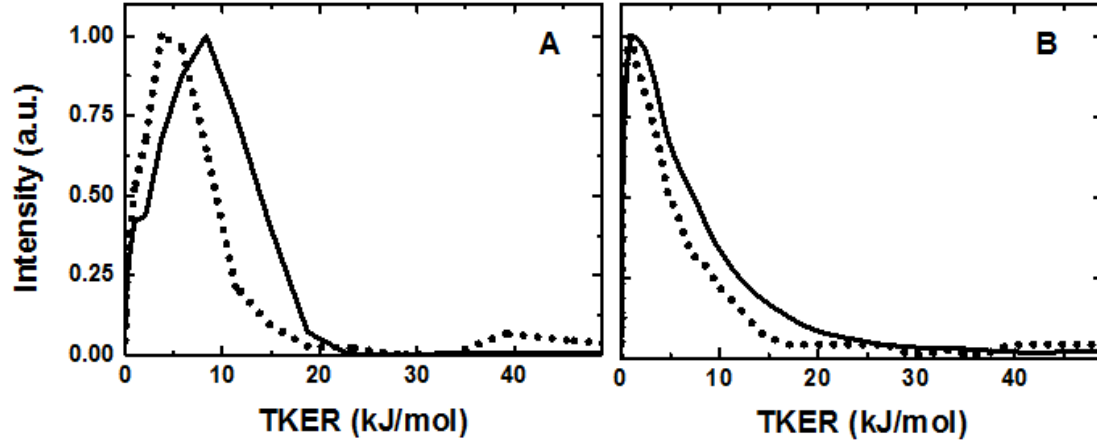


FIG. S.8. Total kinetic energy release distributions deduced from images of $m/z = 41$ fragments from: (A) BCP⁺ (solid line) and AB⁺ (dotted line) photolysis at 355 nm, with the cations prepared by 118 nm ionization and images accumulated using the PImMS camera; and (B) the low energy fragments from BCP (solid line) and AB (dotted line) seen in one colour ionization and photodissociation experiments at 230 nm, with images collected using a higher resolution CCD camera.

S.7 Effects of coherent excitation on photofragment Br atom angular anisotropies

The analysis in Section III.A.1 of recoil velocity anisotropies for Br and Br* atoms assumes that fits of the angular variation of the images to equation (S1) obtain the velocity anisotropy parameter.

$$P(\theta) = \frac{1}{4\pi} \{1 + \beta P_2(\cos\theta)\} \quad (\text{S1})$$

Decomposition of the photoexcitation into parallel and perpendicular transition components is then straightforward because β is an incoherent parameter which is not affected by coherent excitation of more than one excited state or by phase-dependent interferences between dissociating wavepackets.¹

However, the fit parameter of Equation (S1) can subtly differ from the true velocity anisotropy β parameter when there is coherent excitation of two or more excited states. Coherent effects can cause angular momentum polarization of the photofragments which modulates the angular anisotropy of the images when the atomic fragments are probed by polarized light. The resulting angular distribution is better analysed using a fit to the function:

$$P(\theta) = \frac{1}{4\pi} \{1 + \beta_2 P_2(\cos\theta) + \beta_4 P_4(\cos\theta)\} \quad (\text{S2})$$

in which the parameters β_2 and β_4 are influenced by coherent (and hence angular momentum polarization) effects.

We tested the significance of any contributions to our images from coherent photoexcitation by examining the residuals of fits of experimental images to equation (S1). Examples of these fits and residuals are shown in Figure S.9. In the case of the $\text{Br}^*(^2\text{P}_{1/2})$ channel, any angular momentum alignment effects must necessarily vanish because a $j = 1/2$ state cannot show quadrupolar alignment. A fit to equation (S1) should therefore describe the data well and return the true velocity anisotropy parameter, and we observe this behaviour in our Br^* images. However, a $j = 3/2$ state can be aligned, and the $\text{Br}(^2\text{P}_{3/2})$ images show evidence for a weak $\beta_4 P_4(\cos\theta)$ contribution in the fit residuals.

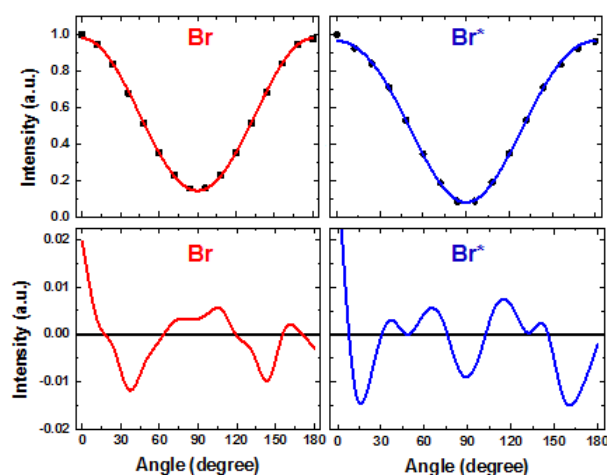


Figure R1: The angular distributions of Br (top, left) and Br^* (top, right) from bromocyclopropane photodissociation. Black points are experimental data. Red (Br) and Blue (Br^*) solid lines are fits to equation (S1). The bottom panels show the residuals of the fits on an expanded scale. The images were obtained from bromocyclopropane photolysis at 240 nm.

If we instead fit the experimental images for Br and Br^* to equation (S2), we obtain the β_2 and β_4 fit parameter values summarized in Table S.2. Any differences between the β_2 values and the β values deduced from fits to equation (S1), which are reproduced in the final column of the table, are indicative of angular momentum polarization in the Br atoms deriving from coherent dynamics.

Fragment imaged	Wavelength (nm)	β_2	β_4	β
Br	235	0.98	-0.1	0.94 ± 0.03
	240	1.3	0.03	1.31 ± 0.01
	245	0.81	-0.13	0.75 ± 0.05
	266	1.10	-0.003	1.11 ± 0.01
Br^*	230	1.48	-0.17	1.48 ± 0.06

	235	1.68	0.003	1.68±0.02
	240	1.50	-0.12	1.51±0.05
	245	1.61	0.04	1.61±0.02
	266	0.62	0.05	0.62±0.01

Table S.2: Anisotropy parameter values obtained from fits of Br and Br* images from UV photolysis of bromocyclopropane. The images were fitted to both equations (R1) (giving the β values in the final column) and (R2) (giving the β_2 and β_4 values).

In the case of the Br* images, β and β_2 values are indistinguishable, as expected for a $j=1/2$ atom. For the Br atom images, there are only modest differences which, together with the small values of β_4 , suggest that neglect of coherent effects will make only a small difference to our analysis in Section III.A.1.

[1] For example, see equation (14) of A.S. Bracker, E.R. Wouters, A.G. Suits and O.S. Vasyutinskii, J. Chem. Phys. **110**, 6749 (1999).